Free interface blade mistuning model: Experimental validation with measured blade variability and contact conditions

Mechanical Systems and Signal Processing 259 (2026) 114829

Contents lists available at ScienceDirect

Mechanical Systems and Signal Processing

journal homepage: www.elsevier.com/locate/ymssp

Full length article

Free interface blade mistuning model: Experimental validation with measured blade variability and contact conditions

Umidjon Usmanov *, Christian Maria Firrone, Giuseppe Battiato

Politecnico di Torino, Corso Duca Degli Abruzzi 24, Turin, 10129, Italy

A R T I C L E I N F O

Communicated by P. Pennacchi

Keywords:
Bladed disks
Mistuning
Reduced order models
Free interface reduction
Vibration analysis

A B S T R A C T

Accurate modeling of mistuning in bladed disks requires a consistent representation of blade-to-blade variability and its impact on the assembled system dynamics. This work presents an experimental validation of a reduced-order modeling approach for mistuned bladed disks, where the variability of individual components is directly derived from measurements. Free–free modal hammer tests are performed on individual blades to quantify the dispersion in natural frequencies arising from manufacturing tolerances and geometric variability. These experimentally measured perturbations are introduced into the reduced-order formulation of the blade component, enabling a physically consistent representation of intrinsic mistuning. The finite element model of the disk is updated based on experimental data, and the full assembly is modeled using a component mode synthesis framework, combining Rubin reduction for the blades and Craig–Bampton reduction for the disk. The assembled bladed disk is experimentally characterized through modal testing, and the numerical predictions are compared against the measured natural frequencies and mode shapes. The results demonstrate that the proposed approach accurately captures the effect of blade variability on the global dynamic behavior. The study highlights the effectiveness of incorporating experimentally derived blade properties into reduced-order model, providing a robust and physically interpretable framework for the analysis of mistuned bladed disks.

1. Introduction

The dynamic behavior of turbine bladed disks is strongly influenced by small variations in the properties of individual blades, making mistuning an inherent aspect of their design [1]. These variations can originate from manufacturing imperfections, variations in material properties, or operational wear, and even minor discrepancies may result in significant increases in vibration amplitudes [2,3]. Such amplification elevates the risk of high-cycle fatigue and introduces additional complexity in predicting system response, as certain blades may exhibit localized vibration levels well beyond those expected in an ideal tuned configuration. Furthermore, mistuning leads to a fundamental modification of the modal behavior of the assembly. The loss of cyclic symmetry induces the frequency splitting of modes that are degenerate in the tuned system and localization of the vibration modes, disrupting the uniform distribution of energy typical of tuned systems [4,5]. Consequently, the overall response becomes governed by a limited subset of blades, whose dynamics cannot be reliably inferred from nominal design assumptions. This effect is particularly critical under forced excitation, where resonance conditions may develop and persist within narrow frequency bands [6]. From a modeling standpoint, capturing blade-to-blade variability with sufficient accuracy often requires high-fidelity finite element models (FEM) of the full assembly, resulting in large-scale computational problems, especially in the context of probabilistic analyses. In addition,

* Corresponding author.
E-mail address: umidjon.usmanov@polito.it (U. Usmanov).

https://doi.org/10.1016/j.ymssp.2026.114829
Received 11 May 2026; Received in revised form 1 July 2026; Accepted 6 August 2026
Available online 17 August 2026

the complex relationship between mistuning parameters and the resulting dynamic response further increases the complexity of analyzing mistuned bladed disks.

Early approaches for analyzing mistuning in bladed disks relies on lumped parameter mass–spring models [2,6–10]. These methods provide an intuitive description of the system dynamics and have been widely used to investigate general trends in mistuned responses. Their main advantage lies in their low computational cost, which makes them well suited for extensive numerical analyses, such as Monte Carlo simulations, and for gaining qualitative physical insight. However, despite their efficiency, these models present important limitations. Their predictions are highly sensitive to model parameters, and they are not able to accurately represent the complex structural behavior of real bladed disks, where geometry, boundary conditions, and modal interactions play a significant role. As the level of detail increases, parameter identification becomes challenging, limiting their applicability to qualitative rather than predictive analyses. An alternative approach consists in deriving reduced-order models (ROMs) directly from finite element formulations, allowing a more accurate representation of the structure while maintaining computational efficiency. Two main classes of ROM techniques are commonly adopted: system-level and component-level approaches [11]. In system-level methods, the response of the mistuned system is expressed as a combination of tuned system modes [12], while component-level approaches perform the reduction at the level of individual substructures, such as blades and disk sectors [13] The latter enables the local introduction of mistuning and preserves a modular framework. Additionally, alternative formulations treat mistuning as a structural modification of the tuned system [14,15], where the mistuned response is obtained by applying correction operators to the dynamic characteristics of the nominal configuration.

System-level reduced-order approaches were initially developed by Yang and Griffin [12], who expressed the mistuned system response as a linear combination of a subset of tuned system modes, thus avoiding full FEM analysis of the mistuned assembly. This concept was further refined by Feiner and Griffin through the Fundamental Model of Mistuning (FMM) [16], which simplifies the formulation by focusing on a single modal family. The FMM requires only the nominal frequencies and the deviations of blade frequencies, providing a compact and efficient framework suitable for large-scale analyses and probabilistic studies. Component-level approaches, on the other hand, perform model reduction at the level of individual substructures, typically separating blades and disk. Early contributions by Castainer et al. [13] introduced formulations based on sector-level component modes, allowing mistuning to be incorporated directly through blade properties. Subsequent developments demonstrated that such models can accurately predict forced responses at a reduced computational cost [17]. Further advancements include interface-based formulations [18] and extensions to more complex configurations such as shrouded disks [19]. The work of Bladh et al. [20,21] introduced advanced reduction techniques, including the Craig–Bampton method and secondary reduction strategies, achieving substantial reductions in model size. Later contributions generalized the framework to account for both stiffness and mass mistuning [22], extended mistuning representations to sector-level variability [23], and proposed modular formulations for the independent treatment of blade and disk variations [24]. An alternative class of methods formulates mistuning as a structural modification of the tuned system [14]. In this framework, the response of the mistuned assembly is obtained directly from the frequency response of the tuned configuration by introducing a modification matrix that accounts for blade variability.

Numerous studies have addressed the development of ROMs for the nonlinear analysis of mistuned bladed disks, with particular emphasis on the incorporation of frictional contact effects. Pourkiaee and Zucca [25] proposed a ROM for systems with shroud friction interfaces, combining Craig–Bampton reduction for the blades with loaded interface modes for the disk, resulting in a compact formulation based on single-sector computations. Mashayekhi et al. [26] introduced the Mistuned-Dual (M-Dual) approach, which integrates the component mistuning method with a Dual CMS framework. By employing free-interface and attachment modes, the method avoids the assembly of full-order matrices and significantly reduces offline computational effort. More recently, Saletti et al. [27] developed a ROM for bladed disks with shroud friction joints under mass mistuning, demonstrating its capability to accurately reproduce nonlinear forced responses in the presence of localized contacts. Long and Chen [28] proposed a Variable-Speed Reduced Order Model (VSROM) for mistuned rotating bladed disks, combining stiffness parameterization as a polynomial with the Component Mode Mistuning method. This approach enables response-based mistuning identification and accurate prediction of both free and forced responses across varying operating conditions.

Despite the significant progress in ROM of mistuned bladed disks, most existing formulations are based on fixed-interface representations, where the physical meaning of the retained modal properties is strongly influenced by boundary conditions and their direct experimental identification is not straightforward. This limitation complicates the incorporation of experimentally measured quantities into ROM. To the best of the authors' knowledge, the use of free-interface reduction strategies as a basis for mistuning analysis has not been extensively explored in this context. The present study builds upon a ROM framework based on free–free component modes, which enables a more direct physical interpretation of the retained dynamic properties and facilitates the introduction of mistuning through experimentally measurable quantities. In addition, the proposed formulation is assessed through experimental validation on a mistuned bladed disk assembly.

In this work, an extended ROM framework for mistuned bladed disks, referred to as the Free-Interface Blade Mistuning (FIBM) method, is developed based on free-interface reduction principles. The Rubin method is applied to the blade component, while the Craig–Bampton method is used for the disk sectors, so that the retained blade modes correspond to free–free conditions. Therefore, the modal parameters of the blades can be directly identified from experimental measurements without dependence on arbitrary boundary constraints. This formulation enables a physically interpretable representation of mistuning through perturbations of experimentally measurable quantities. This representation can be employed in both numerical and experimental applications. In the latter case, it considerably simplifies the mistuning identification process, since the mistuning parameters reduce to the free–free natural frequencies of the individual blades, which can be directly identified through standard modal hammer testing. In addition to the numerical formulation, an experimental campaign is conducted to characterize both the individual components and the

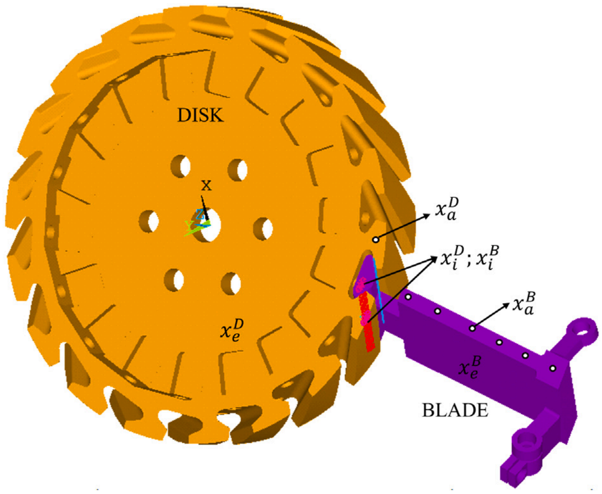

Fig. 1. Schematic representation of the bladed-disk system showing the disk and blade component with the definition of boundary, interface, and auxiliary DOFs.

assembled system. Free–free modal hammer tests are performed on each blade to quantify blade-to-blade variability in natural frequencies, while the disk properties are updated based on experimental measurements. The bladed disk assembly is then tested through modal impact testing to extract its natural frequencies and mode shapes. Validation is carried out by comparing numerical predictions with experimental results in terms of natural frequencies and mode shapes evaluated through the Modal Assurance Criterion (MAC). The results demonstrate that the proposed method is able to accurately reproduce the dynamic behavior of the mistuned assembly while maintaining a significantly reduced computational cost.

The main novelty of the proposed framework lies in the use of free-interface blade modal properties as the mistuning parameters, allowing for their direct experimental identification from standard free–free modal testing of the individual blade components. This work further provides an experimental validation of the complete identification and ROM framework on a mistuned bladed disk accounting for both blade and contact variability.

The remainder of the paper is organized as follows. Section 2 presents the proposed ROM framework for mistuned bladed disks, including the free-interface reduction of the blade, the fixed-interface reduction of the disk sectors, and the analytical assembly procedure. Section 3 describes the experimental campaign, including the characterization of individual components and the testing of the assembled bladed disk. Section 4 presents the numerical analysis based on the proposed ROM. Section 5 is devoted to the comparison between numerical predictions and experimental results in terms of natural frequencies and mode shapes. Finally, Section 6 summarizes the main findings of the study and outlines perspectives for future developments.

2. Methodology

This section introduces the FIBM method for reducing a finite element mistuned bladed disk. The procedure begins with a full FEM of the disk and blade component, representing two physically distinct yet coupled substructures interacting through their shared interfaces. The two substructures are then reduced independently: the disk through the Craig–Bampton method [29] and the blade through the Rubin method [30]. The assembly of the full bladed disk is performed by imposing the compatibility condition at the corresponding interface. Finally, the strategy adopted to introduce blade mistuning is presented and discussed.

With reference to the substructures in Fig. 1, the vectors of DOFs for the disk sector and blade can be partitioned as follows:

$$\boldsymbol{x}^D = \begin{Bmatrix} \boldsymbol{x}_e^D \\ \boldsymbol{x}_i^D \\ \boldsymbol{x}_a^D \end{Bmatrix}, \qquad \boldsymbol{x}^B = \begin{Bmatrix} \boldsymbol{x}_e^B \\ \boldsymbol{x}_i^B \\ \boldsymbol{x}_a^B \end{Bmatrix} \tag{1}$$

In this notation, the superscripts D and B designate the DOFs associated with the disk and the blade, respectively. The subscript i in both vectors identifies the DOFs located at the blade–disk joint *interface* (Fig. 1). The subscript a denotes the *accessory* DOFs, meaning those not directly participating in the interface or structural coupling. The partitions marked with the subscript e in both vectors correspond to the *excess* DOFs, namely those not retained as master DOFs in the applied reduction procedures. In addition, each subscript implicitly defines the dimensionality of the corresponding partition; for instance, the subscript i in $\boldsymbol{x}_i^D$ specifies that the vector has size n_i^D. By following the partitioning indicated in Eq. (1), the FE mass and stiffness matrices for the disk sector and blade are written as:

$$\boldsymbol{K}^D = \begin{bmatrix} \boldsymbol{K}_{ee}^D & \boldsymbol{K}_{ei}^D & \boldsymbol{K}_{ea}^D \\ \boldsymbol{K}_{ie}^D & \boldsymbol{K}_{ii}^D & \boldsymbol{K}_{ia}^D \\ \boldsymbol{K}_{ae}^D & \boldsymbol{K}_{ai}^D & \boldsymbol{K}_{aa}^D \end{bmatrix}, \qquad \boldsymbol{M}^D = \begin{bmatrix} \boldsymbol{M}_{ee}^D & \boldsymbol{M}_{ei}^D & \boldsymbol{M}_{ea}^D \\ \boldsymbol{M}_{ie}^D & \boldsymbol{M}_{ii}^D & \boldsymbol{M}_{ia}^D \\ \boldsymbol{M}_{ae}^D & \boldsymbol{M}_{ai}^D & \boldsymbol{M}_{aa}^D \end{bmatrix} \tag{2}$$

$$\boldsymbol{K}^B = \begin{bmatrix} \boldsymbol{K}^B_{ee} & \boldsymbol{K}^B_{ei} & \boldsymbol{K}^B_{ea} \\ \boldsymbol{K}^B_{ie} & \boldsymbol{K}^B_{ii} & \boldsymbol{K}^B_{ia} \\ \boldsymbol{K}^B_{ae} & \boldsymbol{K}^B_{ai} & \boldsymbol{K}^B_{aa} \end{bmatrix}, \qquad \boldsymbol{M}^B = \begin{bmatrix} \boldsymbol{M}^B_{ee} & \boldsymbol{M}^B_{ei} & \boldsymbol{M}^B_{ea} \\ \boldsymbol{M}^B_{ie} & \boldsymbol{M}^B_{ii} & \boldsymbol{M}^B_{ia} \\ \boldsymbol{M}^B_{ae} & \boldsymbol{M}^B_{ai} & \boldsymbol{M}^B_{aa} \end{bmatrix} \tag{3}$$

This structured partitioning provides a clear distinction between the physically meaningful DOFs that must be retained to preserve the system behavior, namely *boundary* DOFs, and those that can be systematically reduced, i.e., *excess* DOFs. For both the blade and disk components, the boundary sets $\boldsymbol{x}_b^B$ and $\boldsymbol{x}_b^D$ typically include the DOFs at the blade–root interface and the accessory coordinates. Excess DOFs will be condensed through the reduction steps presented in the following sections.

$$\boldsymbol{x}_b^B = \begin{Bmatrix} \boldsymbol{x}_i^B \\ \boldsymbol{x}_a^B \end{Bmatrix} \qquad \boldsymbol{x}_b^D = \begin{Bmatrix} \boldsymbol{x}_i^D \\ \boldsymbol{x}_a^D \end{Bmatrix} \tag{4}$$

2.1. Disk reduction

The disk is reduced using the CB-CMS method [29], in which the displacement field of the excess DOFs is represented as a linear combination of two complementary sets of component modes. The first set, referred to as *constraint* (or *static*) modes and denoted by $\boldsymbol{\Psi}_{be}$, corresponds to the static deformation patterns obtained by applying a unit displacement at a boundary DOF while keeping all other boundary DOFs fixed. The second set, denoted by $\boldsymbol{\Phi}_{ke}$, is composed of a truncated number n_k (with $n_k \ll n_e^D$) of *fixed-interface normal modes*, which capture the dynamic flexibility of the substructure under the assumption that the boundary displacement vector $\boldsymbol{x}_b^D$ is fully constrained. By construction, the Craig–Bampton reduction method relies on the partitioning of the FE mass and stiffness matrices with respect to boundary and exceeding DOFs. Considering the DOFs partitioning defined in Eq. (4), the mass and stiffness FE matrices of Eqs. (2) can be expressed in a more compact form as:

$$\boldsymbol{K}^D = \begin{bmatrix} \boldsymbol{K}^D_{ee} & \boldsymbol{K}^D_{eb} \\ \boldsymbol{K}^D_{be} & \boldsymbol{K}^D_{bb} \end{bmatrix}, \qquad \boldsymbol{M}^D = \begin{bmatrix} \boldsymbol{M}^D_{ee} & \boldsymbol{M}^D_{eb} \\ \boldsymbol{M}^D_{be} & \boldsymbol{M}^D_{bb} \end{bmatrix} \tag{5}$$

The application of the CB method leads to the following approximation of the physical displacement vector $\boldsymbol{x}^D$

$$\boldsymbol{x}^D = \begin{Bmatrix} \boldsymbol{x}_e^D \\ \boldsymbol{x}_b^D \end{Bmatrix} = \begin{bmatrix} \boldsymbol{\Phi}^D_{ke} & \boldsymbol{\Psi}^D_{be} \\ \boldsymbol{0}_{bk} & \boldsymbol{I}_{bb} \end{bmatrix} \begin{Bmatrix} \boldsymbol{\eta}_k^D \\ \boldsymbol{x}_b^D \end{Bmatrix} = \boldsymbol{R}^D_{CB}\, \boldsymbol{q}^D_{CB} \tag{6}$$

where $\boldsymbol{R}^D_{CB}$ is the CB reduction matrix, and $\boldsymbol{\eta}_k^D$ is the vector of modal amplitudes associated with the retained fixed-interface normal modes. The vector $\boldsymbol{q}^D_{CB} = \{(\boldsymbol{x}_b^D)^T\ (\boldsymbol{\eta}_k^D)^T\}^T$ thus represents the reduced generalized coordinate vector in the CB formulation.

The reduction basis $\boldsymbol{R}^D_{CB}$ is then used to project the full mass and stiffness matrices, $\boldsymbol{M}^D$ and $\boldsymbol{K}^D$, onto the reduced space, yielding the reduced matrices $\tilde{\boldsymbol{M}}^D$ and $\tilde{\boldsymbol{K}}^D$.

$$\tilde{\boldsymbol{K}}^D = (\boldsymbol{R}^D_{CB})^T \cdot \boldsymbol{K}^D \cdot \boldsymbol{R}^D_{CB} = \begin{bmatrix} \boldsymbol{\Lambda}^D & \boldsymbol{0} \\ \boldsymbol{0} & \boldsymbol{\kappa}^D_{bb} \end{bmatrix}, \qquad \tilde{\boldsymbol{M}}^D = (\boldsymbol{R}^D_{CB})^T \cdot \boldsymbol{M}^D \cdot \boldsymbol{R}^D_{CB} = \begin{bmatrix} \boldsymbol{I}_k & (\boldsymbol{\mu}^D_{be})^T \\ \boldsymbol{\mu}^D_{be} & \boldsymbol{\mu}^D_{bb} \end{bmatrix} \tag{7}$$

$$\begin{aligned} \boldsymbol{\kappa}^D_{bb} &= \boldsymbol{K}^D_{bb} \cdot \boldsymbol{\Psi}^D_{be} + \boldsymbol{K}^D_{be}, \\ \boldsymbol{\mu}^D_{be} &= (\boldsymbol{\Psi}^D_{be})^T \cdot \boldsymbol{M}^D_{ee} \cdot \boldsymbol{\Psi}^D_{be} + \boldsymbol{M}^D_{eb} \cdot \boldsymbol{\Psi}^D_{be} + \boldsymbol{M}^D_{be}, \\ \boldsymbol{\mu}^D_{bb} &= (\boldsymbol{\Psi}^D_{be})^T \cdot \left(\boldsymbol{M}^D_{ee} \cdot \boldsymbol{\Psi}^D_{be} + \boldsymbol{M}^D_{eb}\right) + (\boldsymbol{M}^D_{be})^T \cdot \boldsymbol{\Psi}^D_{be} + \boldsymbol{M}^D_{bb} \end{aligned} \tag{8}$$

2.2. Blade reduction

The Rubin free-interface reduction method is adopted in this work for the reduction of the blade component [30]. The reduction basis in the Rubin method is constructed from two complementary sets of modes. The first set, *residual attachment modes* $\boldsymbol{\Psi}_r$, is obtained as the difference between the total static flexibility of the substructure and the flexibility represented by the retained dynamic modes. For further details on the computation of the residual attachment modes, the reader is referred to [31]. The second set consists of *free-interface normal modes* $\boldsymbol{\Phi}_f$, which are computed with the interface DOFs left unconstrained. These modes capture the free–free vibration modes of the component and can also be directly correlated with experimental modal tests conducted under free boundary conditions. In addition, when a component exhibits rigid body motions, a third set of *rigid body modes* $\boldsymbol{\Phi}_r$ may be incorporated into the basis to guarantee a complete representation. In the most general case, the displacement vector of the blade can be approximated as

$$\boldsymbol{x}^B \approx \boldsymbol{\Phi}^B_r \boldsymbol{\eta}^B_r + \boldsymbol{\Phi}^B_f \boldsymbol{\eta}^B_f + \boldsymbol{\Psi}^B_r \boldsymbol{g}^B_b = \begin{bmatrix} \boldsymbol{\Phi}^B_r & \boldsymbol{\Phi}^B_f & \boldsymbol{\Psi}^B_r \end{bmatrix} \begin{Bmatrix} \boldsymbol{\eta}^B_r \\ \boldsymbol{\eta}^B_f \\ \boldsymbol{g}^B_b \end{Bmatrix} = \boldsymbol{R}^B_R\, \boldsymbol{q}^B_R \tag{9}$$

where $\boldsymbol{R}^B_R$ is the Rubin reduction matrix and $\boldsymbol{q}^B_R = \{(\boldsymbol{\eta}^B_r)^T\ (\boldsymbol{\eta}^B_f)^T\ (\boldsymbol{g}^B_b)^T\}^T$ is the corresponding reduced generalized coordinate vector in the Rubin formulation. The vectors $\boldsymbol{\eta}^B_r$ and $\boldsymbol{\eta}^B_f$ are the reduced set of generalized coordinates associated with the rigid body and free-interface modes, respectively, while $\boldsymbol{g}^B_b$ contains the forces acting at the boundary DOFs. By projecting the blade FE mass and stiffness matrices onto the space spanned by the columns of $\boldsymbol{R}^B_R$, the following reduced matrices are obtained:

$$\bar{\boldsymbol{M}}^B = (\boldsymbol{R}^B_R)^T \cdot \boldsymbol{M}^B \cdot \boldsymbol{R}^B_R = \begin{bmatrix} \boldsymbol{I} & \boldsymbol{0} & \boldsymbol{0} \\ \boldsymbol{0} & \boldsymbol{I} & \boldsymbol{0} \\ \boldsymbol{0} & \boldsymbol{0} & \boldsymbol{M}^B_{r,b} \end{bmatrix}, \qquad \bar{\boldsymbol{K}}^B = (\boldsymbol{R}^B_R)^T \cdot \boldsymbol{K}^B \cdot \boldsymbol{R}^B_R = \begin{bmatrix} \boldsymbol{0} & \boldsymbol{0} & \boldsymbol{0} \\ \boldsymbol{0} & \boldsymbol{\Omega}^2_f & \boldsymbol{0} \\ \boldsymbol{0} & \boldsymbol{0} & \boldsymbol{G}^B_{r,b} \end{bmatrix} \tag{10}$$

where $\boldsymbol{M}^B_{r,b}$ and $\boldsymbol{G}^B_{r,b}$ are the interface inertia and flexibility associated with the residual flexibility modes at the boundary. These can be written as:

$$\boldsymbol{G}^B_{r,b} = (\boldsymbol{\Psi}^B_r)^T \cdot \boldsymbol{K}^B \cdot \boldsymbol{\Psi}^B_r, \qquad \boldsymbol{M}^B_{r,b} = (\boldsymbol{\Psi}^B_r)^T \cdot \boldsymbol{M}^B \cdot \boldsymbol{\Psi}^B_r \tag{11}$$

The reduced matrices obtained with the Rubin free-interface approach possess a clear and physically interpretable structure. As expressed in Eq. (10), the reduced blade stiffness matrix $\bar{\boldsymbol{K}}^B$ contains a diagonal block with the squared free-interface natural frequencies, $\boldsymbol{\Omega}^2_f$, which is independent of the choice of boundary DOFs.

The Rubin reduction does not directly lead to a standard super-element formulation, since the boundary DOFs are expressed in terms of interface forces $\boldsymbol{g}^B_b$ rather than interface displacements $\boldsymbol{x}^B_b$, as shown in Eq. (9). This formulation, however, can already be employed if one prefers to work in a *dual* form, where the assembly is performed by imposing equilibrium conditions on the boundary forces using Lagrangian multipliers [32]. An alternative option is the *primal* form of assembly, where compatibility conditions are imposed on the displacements and the equilibrium condition is automatically satisfied by definition. Therefore, a secondary transformation is required to convert the boundary forces into boundary displacements [33]. The authors choose an assembly in a primal form. Such a transformation is found by pre-multiplying Eq. (9) by the boolean matrix $\boldsymbol{A}$, which selects the boundary DOFs $\boldsymbol{x}^B_b$ from the full displacement field $\boldsymbol{x}^B$:

$$\boldsymbol{x}^B_b = \boldsymbol{A}\boldsymbol{x}^B = \boldsymbol{A}(\boldsymbol{\Phi}^B_r\,\boldsymbol{\eta}^B_r + \boldsymbol{\Phi}^B_f\,\boldsymbol{\eta}^B_f + \boldsymbol{\Psi}^B_r\,\boldsymbol{g}^B_b) \tag{12}$$

From this equation, the boundary force DOFs can be expressed as:

$$\boldsymbol{g}^B_b = \boldsymbol{K}^B_{r,b}(\boldsymbol{x}^B_b - \boldsymbol{A}\boldsymbol{\Phi}^B_r\boldsymbol{\eta}^B_r - \boldsymbol{A}\boldsymbol{\Phi}^B_f\boldsymbol{\eta}^B_f) \tag{13}$$

In this expression, $\boldsymbol{K}^B_{r,b}$ is the residual stiffness corresponding to the boundary DOFs, which can be obtained by applying the matrix $\boldsymbol{A}$ to the residual flexibility matrix, i.e., matrix of residual attachment modes, and taking an inverse:

$$\boldsymbol{K}^B_{r,b} = \left(\boldsymbol{A} \cdot \boldsymbol{\Psi}^B_r\right)^{-1} \tag{14}$$

Therefore, the secondary transformation can be expressed as:

$$\begin{Bmatrix} \boldsymbol{\eta}^B_r \\ \boldsymbol{\eta}^B_f \\ \boldsymbol{g}^B_b \end{Bmatrix} = \begin{bmatrix} \boldsymbol{I} & \boldsymbol{0} & \boldsymbol{0} \\ \boldsymbol{0} & \boldsymbol{I} & \boldsymbol{0} \\ -\boldsymbol{K}^B_{r,b}\boldsymbol{A}\boldsymbol{\Phi}^B_r & -\boldsymbol{K}^B_{r,b}\boldsymbol{A}\boldsymbol{\Phi}^B_f & \boldsymbol{K}^B_{r,b} \end{bmatrix} \begin{Bmatrix} \boldsymbol{\eta}^B_r \\ \boldsymbol{\eta}^B_f \\ \boldsymbol{x}^B_b \end{Bmatrix} = \boldsymbol{T}^B_2 \begin{Bmatrix} \boldsymbol{\eta}^B_r \\ \boldsymbol{\eta}^B_f \\ \boldsymbol{x}^B_b \end{Bmatrix} \tag{15}$$

The final reduced mass and stiffness matrices can be obtained from the subsequent application of the reduction steps described from Eq. (10) to Eq. (15):

$$\tilde{\boldsymbol{M}}^B = (\boldsymbol{T}^B_2)^T \cdot \bar{\boldsymbol{M}}^B \cdot \boldsymbol{T}^B_2, \qquad \tilde{\boldsymbol{K}}^B = (\boldsymbol{T}^B_2)^T \cdot \bar{\boldsymbol{K}}^B \cdot \boldsymbol{T}^B_2 \tag{16}$$

$$\tilde{\boldsymbol{M}}^B = \begin{bmatrix} \boldsymbol{I} + (\boldsymbol{\Phi}^B_{r|b})^T\,\hat{\boldsymbol{M}}^B_r\,\boldsymbol{\Phi}^B_{r|b} & (\boldsymbol{\Phi}^B_{r|b})^T\,\hat{\boldsymbol{M}}^B_r\,\boldsymbol{\Phi}^B_{f|b} & -(\boldsymbol{\Phi}^B_{r|b})^T\,\hat{\boldsymbol{M}}^B_r \\ (\boldsymbol{\Phi}^B_{f|b})^T\,\hat{\boldsymbol{M}}^B_r\,\boldsymbol{\Phi}^B_{r|b} & \boldsymbol{I} + (\boldsymbol{\Phi}^B_{f|b})^T\,\hat{\boldsymbol{M}}^B_r\,\boldsymbol{\Phi}^B_{f|b} & -(\boldsymbol{\Phi}^B_{f|b})^T\,\hat{\boldsymbol{M}}^B_r \\ -\hat{\boldsymbol{M}}^B_r\,\boldsymbol{\Phi}^B_{r|b} & -\hat{\boldsymbol{M}}^B_r\,\boldsymbol{\Phi}^B_{f|b} & \hat{\boldsymbol{M}}^B_r \end{bmatrix} \tag{17}$$

$$\tilde{\boldsymbol{K}}^B = \begin{bmatrix} (\boldsymbol{\Phi}^B_{r|b})^T\,\boldsymbol{K}^B_{r,b}\,\boldsymbol{\Phi}^B_{r|b} & (\boldsymbol{\Phi}^B_{r|b})^T\,\boldsymbol{K}^B_{r,b}\,\boldsymbol{\Phi}^B_{f|b} & -(\boldsymbol{\Phi}^B_{r|b})^T\,\boldsymbol{K}^B_{r,b} \\ (\boldsymbol{\Phi}^B_{f|b})^T\,\boldsymbol{K}^B_{r,b}\,\boldsymbol{\Phi}^B_{r|b} & \boldsymbol{\Omega}^2_f + (\boldsymbol{\Phi}^B_{f|b})^T\,\boldsymbol{K}^B_{r,b}\,\boldsymbol{\Phi}^B_{f|b} & -(\boldsymbol{\Phi}^B_{f|b})^T\,\boldsymbol{K}^B_{r,b} \\ -\boldsymbol{K}^B_{r,b}\,\boldsymbol{\Phi}^B_{r|b} & -\boldsymbol{K}^B_{r,b}\,\boldsymbol{\Phi}^B_{f|b} & \boldsymbol{K}^B_{r,b} \end{bmatrix} \tag{18}$$

where $\hat{\boldsymbol{M}}^B_r = (\boldsymbol{K}^B_{r,b})^T \cdot \boldsymbol{M}^B_{r,b} \cdot \boldsymbol{K}^B_{r,b}$ is the condensed residual inertia matrix associated with the residual flexibility modes at the interface. $\boldsymbol{\Phi}^B_{r|b} = \boldsymbol{A} \cdot \boldsymbol{\Phi}^B_r$ and $\boldsymbol{\Phi}^B_{f|b} = \boldsymbol{A} \cdot \boldsymbol{\Phi}^B_f$ denote the partitions of the rigid body and free-interface modes related to the boundary DOFs.

2.3. Mistuning modeling

Mistuning is incorporated at the modal level by introducing perturbations to the eigenvalues, i.e., square of the free-interface natural frequencies, of the blade component. These correspond to the diagonal entries in the submatrix $\boldsymbol{\Omega}^2_f$, in Eq. (18). The effect of mistuning is therefore embedded directly into the reduced formulation without modifying the reduction basis or the assembly procedure. As a consequence, the global mass and stiffness matrices preserve a closed analytical structure, since only a specific partition of the stiffness matrix is affected by the introduced perturbations. The formulation relies on two key assumptions. First, the mode shapes of the mistuned substructure are assumed to remain unchanged with respect to the tuned configuration, so that mistuning is represented solely through perturbations of the eigenvalues. Second, the disk is considered nominally tuned, so the mistuning is introduced exclusively at the blade level. Under these assumptions, the variability of the system is fully captured through blade-to-blade differences in the modal properties. This strategy provides a simple and efficient way to control blade-to-blade variability and is strongly compatible with experimental data, as free-interface natural frequencies can be directly identified through modal testing and readily incorporated into the ROM framework. As a direct consequence, the mistuning identification problem reduces to the identification of the blade properties solely in terms of their free-interface natural frequencies, i.e., under free–free boundary conditions.

In the reduced stiffness matrix (Eq. (18)), the blade free-interface natural frequencies appear explicitly in the diagonal block, corresponding to the (2,2) partition of the matrix:

$$\boldsymbol{\Omega}_f^2 = \mathrm{diag}\left(\omega_{f,1}^2,\ \omega_{f,2}^2,\ \dots,\ \omega_{f,m}^2\right) \tag{19}$$

where $\omega_{f,i}$ denotes the ith free-interface natural frequency of the blade, and m is the number of retained free-interface modes in the reduction basis.

In an ideally tuned configuration, all blades share identical dynamic properties, leading to identical reduced stiffness matrices and identical free-interface natural frequencies. However, in real structures, mistuning is unavoidable, resulting in blade-to-blade variations. In the present formulation, mistuning is introduced by perturbing the square of the free-interface natural frequencies within the eigenvalue matrix, thereby assigning a distinct dynamic signature to each blade.

Accordingly, the eigenvalue matrix of the jth perturbed blade can be expressed as

$$(\boldsymbol{\Omega}_f^{(j)})^2 = \mathrm{diag}\left(\omega_{f,1}^2(1+\delta_1^{(j)}),\ \omega_{f,2}^2(1+\delta_2^{(j)}),\ \dots,\ \omega_{f,m}^2(1+\delta_m^{(j)})\right), \tag{20}$$

where $\delta_i^{(j)}$ represents the relative perturbation associated with the ith free-interface mode of the jth blade.

This formulation is highly flexible since each blade can be assigned its own mistuning pattern, and each retained mode on a given blade can be perturbed independently. In numerical applications, the perturbations can be readily obtained by performing numerical modal analysis on the blade components and extracting the corresponding natural frequencies. In contrast, in the experimental case, the number of modes that can be perturbed is limited by the number of free-interface modes that can be reliably identified from measurements.

2.4. Bladed disk assembly

The full bladed-disk ROM is obtained by imposing compatibility between the blade–root DOFs, i.e., $\boldsymbol{x}_i^D$ and $\boldsymbol{x}_i^{B,N}$, belonging between disk ROM and the reduced blade components:

$$\begin{Bmatrix} \boldsymbol{\eta}_k^D \\ \boldsymbol{x}_i^D \\ \boldsymbol{x}_a^D \\ \boldsymbol{\eta}_r^{B,N} \\ \boldsymbol{\eta}_f^{B,N} \\ \boldsymbol{x}_i^{B,N} \\ \boldsymbol{x}_a^{B,N} \end{Bmatrix} = \begin{bmatrix} \mathbf{1} & \mathbf{0} & \mathbf{0} & \mathbf{0} & \mathbf{0} & \mathbf{0} \\ \mathbf{0} & \mathbf{1} & \mathbf{0} & \mathbf{0} & \mathbf{0} & \mathbf{0} \\ \mathbf{0} & \mathbf{0} & \mathbf{1} & \mathbf{0} & \mathbf{0} & \mathbf{0} \\ \mathbf{0} & \mathbf{0} & \mathbf{0} & \mathbf{1} & \mathbf{0} & \mathbf{0} \\ \mathbf{0} & \mathbf{0} & \mathbf{0} & \mathbf{0} & \mathbf{1} & \mathbf{0} \\ \mathbf{0} & \mathbf{1} & \mathbf{0} & \mathbf{0} & \mathbf{0} & \mathbf{0} \\ \mathbf{0} & \mathbf{0} & \mathbf{0} & \mathbf{0} & \mathbf{0} & \mathbf{1} \end{bmatrix} \begin{Bmatrix} \boldsymbol{\eta}_k^D \\ \boldsymbol{x}_i \\ \boldsymbol{x}_a^D \\ \boldsymbol{\eta}_r^{B,N} \\ \boldsymbol{\eta}_f^{B,N} \\ \boldsymbol{x}_a^{B,N} \end{Bmatrix} = \boldsymbol{A}_{bd}\, \boldsymbol{q}_{bd} \tag{21}$$

where $\boldsymbol{A}_{bd}$ is the global assembly matrix, and $\boldsymbol{q}_{bd} = \{(\boldsymbol{\eta}_k^D)^T\ (\boldsymbol{x}_i)^T\ (\boldsymbol{x}_a^D)^T\ (\boldsymbol{\eta}_r^{B,N})^T\ (\boldsymbol{\eta}_f^{B,N})^T\ (\boldsymbol{x}_a^{B,N})^T\}^T$ represents the reduced generalized coordinate vector. The superscript B,N indicates that the corresponding quantities refer to all N blades of the assembly, where N denotes the total number of blades.

Eq. (21) refers to an idealized assembly condition, where the contact between the blade and disk is assumed to be fully established over the entire nominal interface. Under this assumption, compatibility is enforced across all interface DOFs, implying that all nodes in the contact region are in contact. In practice, however, the contact condition may deviate from this ideal scenario. Due to geometric variations and assembly imperfections, only a subset of the interface region may be effectively in contact, while others remain detached. This phenomenon is commonly referred in the literature as contact mistuning and represents an additional source of mistuning, complementing the intrinsic blade-to-blade variability [34–38]. Therefore, in the presence of contact mistuning, compatibility condition is enforced only at the nodes corresponding to the contacting region of the interface, leading to the global assembly matrix $\boldsymbol{A}_{bd}$ different from that of the ideal case. In particular, the partitions of $\boldsymbol{A}_{bd}$ corresponding to the $(2,2)$ and $(6,2)$ positions are affected, as they must be redefined to impose compatibility only on the actual contact nodes.

The corresponding mass and stiffness matrices for the assembled bladed disk are

$$\boldsymbol{K}^{BD} = (\boldsymbol{A}_{bd})^T \begin{bmatrix} \tilde{\boldsymbol{K}}^D & \mathbf{0} \\ \mathbf{0} & \tilde{\boldsymbol{K}}^B \end{bmatrix} \boldsymbol{A}_{bd}, \qquad \boldsymbol{M}^{BD} = (\boldsymbol{A}_{bd})^T \begin{bmatrix} \tilde{\boldsymbol{M}}^D & \mathbf{0} \\ \mathbf{0} & \tilde{\boldsymbol{M}}^B \end{bmatrix} \boldsymbol{A}_{bd} \tag{22}$$

At this stage, once the full bladed disk assembly has been obtained in physical coordinates, the user has the possibility to apply an additional reduction of the blade–root interface DOF using the Gram–Schmidt interface reduction approach [39]. This step is optional and depends on the number of interface DOFs retained at the blade root. If the number of these DOFs is already sufficiently small, the model can be considered complete, and no further reduction is required. However, if the interface DOFs remain relatively large, applying this additional reduction provides a more compact representation.

3. Experimental activity

This section presents the experimental activity carried out to characterize both the individual components and the assembled bladed disk. The latter consists of an academic bladed disk specifically designed and employed in laboratory testing activities. First, the disk and the 18 blades are tested separately under free conditions using modal hammer excitation and a laser Doppler vibrometer

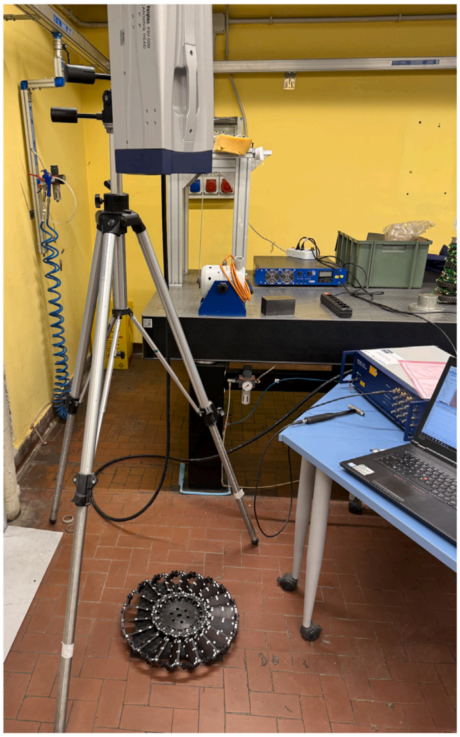

Fig. 2. Experimental setup for modal testing using LDV and impact hammer under free–free conditions.

(LDV) acquisition system. The measured responses are post-processed through experimental modal analysis (EMA), employing the Least Squares Rational Fractions (LSRF) curve-fitting technique to identify natural frequencies and mode shapes. Subsequently, the full assembly is constructed by mounting the blades into the disk slots and applying a controlled bolt preload at the interface. Finally, modal hammer testing is performed on the assembled system to extract its modal parameters for validation purposes.

3.1. Component analysis

Fig. 3 illustrates the components under investigation, i.e., disk (Fig. 3(a)) and single representative blade (Fig. 3(b)). These were tested under free–free boundary conditions, which were achieved by placing the specimens on soft foam supports to minimize boundary constraints and approximate unconstrained behavior. The response measurements were acquired using a LDV, specifically the Polytec PSV-500 system. Excitation was provided through impact hammer testing, using two different hammers to account for the difference in size and mass between the components. In both cases, the hammer was equipped with a force transducer at its tip, allowing the measurement of the input force. Fig. 2 shows the experimental setup used for the modal testing, including the LDV system, the impact hammer, and the data acquisition hardware. The bladed disk assembly is positioned on the floor under free–free boundary conditions during the measurements. For the disk, one acquisition point per sector was considered, resulting in a total of 18 measurement points over the full disk. For each blade, 10 acquisition points were defined to adequately capture the mode shapes.

The total number of blades considered in this study is 18, and they are not perfectly identical. In addition to minor variations due to manufacturing tolerances, blade-to-blade variability arises from specific geometric features, such as the presence of fillets at certain edges and a small cut on the flank region. These geometric variations introduce an additional source of mistuning, beyond the intrinsic variability of the components. Based on these features, the blades can be classified into three groups: type-A, type-B, and type-C. The classification is defined according to three geometric features: the presence or absence of a fillet at the root, a fillet at the flank, and a cut at the flank. Among the 18 blades, one belongs to type-A, three to type-B, and the remaining blades (the majority) to type-C. A summary of the classification and the corresponding blade indices is provided in Table 1. The geometrical differences associated with each feature are further illustrated in Fig. 4.

The measured frequency bandwidth is set to 10 kHz for blade and 6 kHz for the disk. These values ensure reliable identification of the dynamic response using impact hammer excitation without significant noise contamination. An example of the measured FRF for both the disk and a representative blade, obtained at a selected measurement point, is shown in Fig. 5. The measurements are performed in the direction orthogonal to the surface of the components, corresponding to the out-of-plane direction.

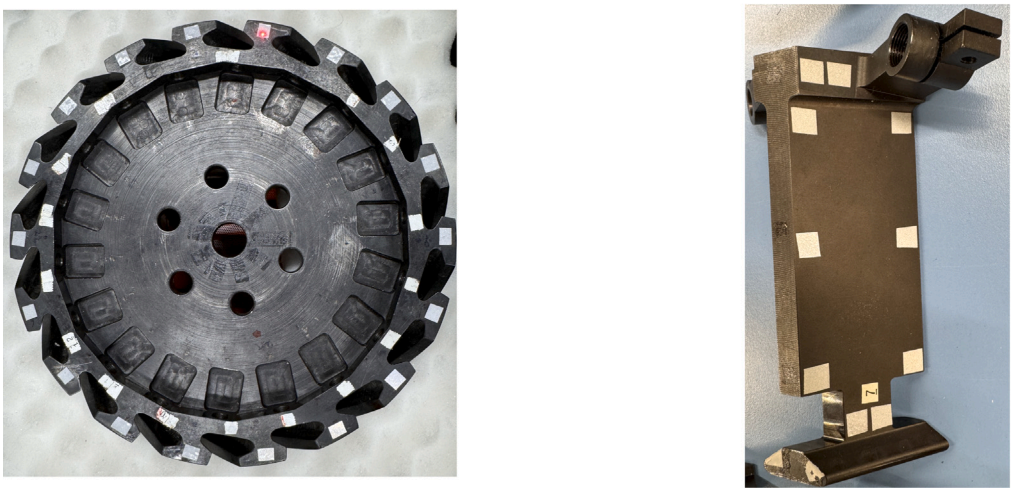

(a) (b)

Fig. 3. Components under investigation: (a) disk; (b) blade.

Table 1
Classification of blade geometries based on key features.

Category	Fillet at root	Fillet at flank	Cut at flank	Blade indices
Type-A	No	No	No	2
Type-B	Yes	No	Yes	5, 11, 16
Type-C	Yes	Yes	Yes	1, 3, 4, 6, 7, 8, 9, 10, 12, 13, 14, 15, 17, 18

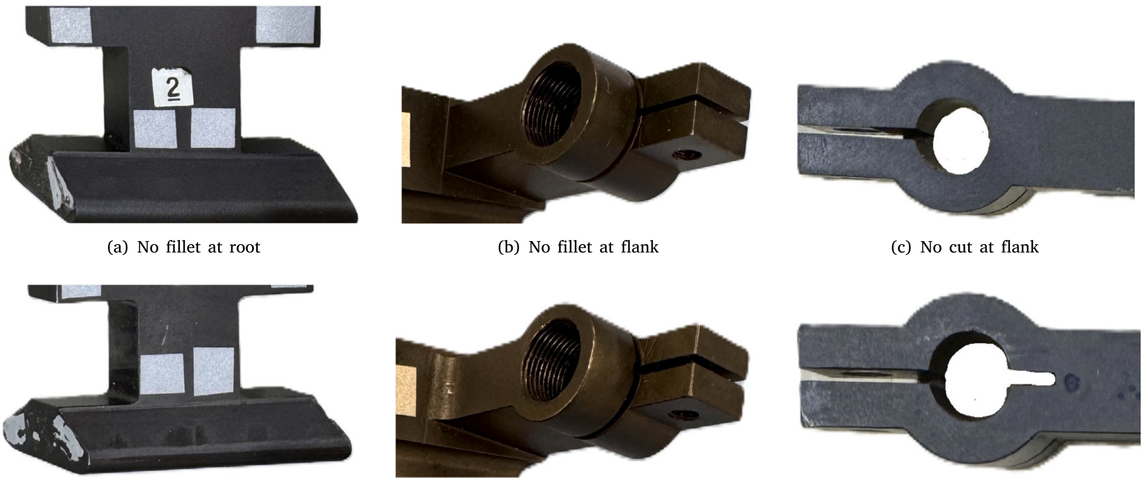

(a) No fillet at root (b) No fillet at flank (c) No cut at flank

(d) Fillet at root (e) Fillet at flank (f) Cut at flank

Fig. 4. Geometrical features used for blade classification: absence (top row) and presence (bottom row) of fillets and cut.

After acquiring the measurements, the FRFs are post-processed by means of EMA, using the LSRF technique [40]. This method approximates the measured FRFs in the frequency domain through a rational function, allowing the extraction of the modal parameters, namely natural frequencies, damping ratios, and mode shapes.

In the LSRF framework, the measured FRF is approximated as

$$H(\omega) \approx \frac{N(\omega)}{D(\omega)}, \tag{23}$$

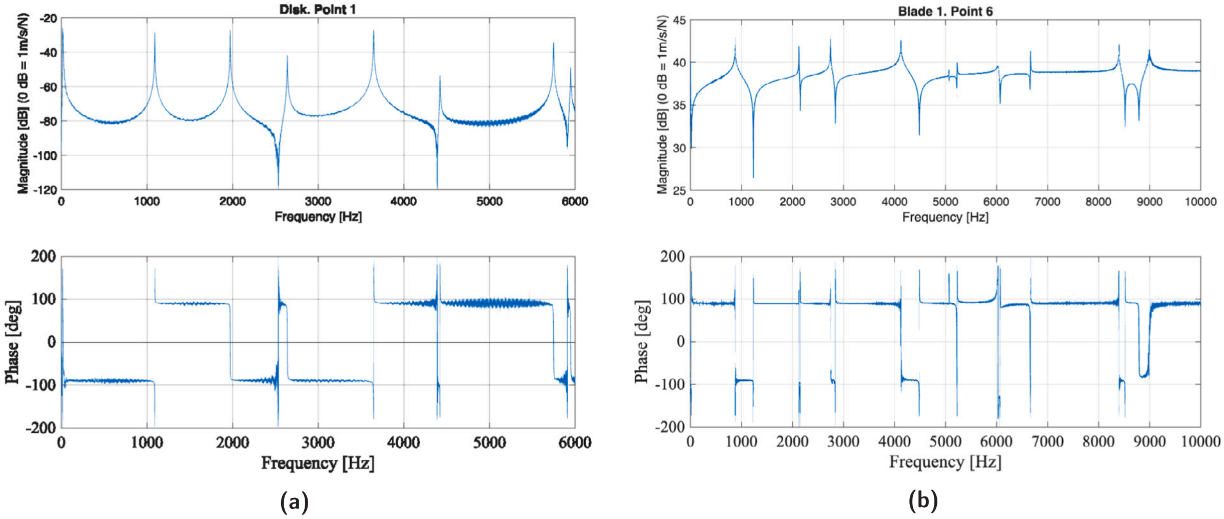

Fig. 5. Measured frequency response functions (FRFs) for (a) the disk and (b) a blade at representative points.

Table 2
Identified natural frequencies and corresponding nodal diameters of the disk.

Mode	Frequency [Hz]	Nodal diameter
1	1090.6	2
2	1971.1	0
3	2638.1	3
4	3647.6	1
5	4421.5	4
6	5747.6	2
7	5947.9	0

where $N(\omega)$ and $D(\omega)$ are polynomial functions of the angular frequency. More generally, for a multi-DOF system, the FRF can be expressed in pole-residue form as

$$H_{pq}(\omega) = \sum_{r=1}^{n_m} \left(\frac{A_{pq}^{(r)}}{j\omega - \lambda_r} + \frac{\bar{A}_{pq}^{(r)}}{j\omega - \bar{\lambda}_r} \right) + \frac{L_{pq}}{(j\omega)^2} + \frac{U_{pq}}{1}, \tag{24}$$

where $H_{pq}(\omega)$ is the FRF between excitation point q and response point p, λ_r are the complex poles, $A_{pq}^{(r)}$ are the corresponding residues, and L_{pq} and U_{pq} represent the low- and high-frequency residual terms, respectively.

Once the poles are identified, the natural frequencies and damping ratios are obtained from

$$\lambda_r = -\zeta_r \omega_{n,r} + j\,\omega_{n,r}\sqrt{1-\zeta_r^2}, \tag{25}$$

from which

$$\omega_{n,r} = |\lambda_r|, \qquad \zeta_r = -\frac{\Re(\lambda_r)}{|\lambda_r|}. \tag{26}$$

Further details on the theoretical foundations of the experimental modal analysis procedure can be found in [41,42].

To distinguish the physical modes from spurious numerical poles, a stabilization diagram is constructed by repeating the identification over increasing model orders. The physical modes were selected by tracking the poles over successive model orders and identifying those forming continuous stable branches in terms of frequency and damping. An example of a stabilization diagram is shown in Fig. 6.

As a result of the EMA, 11 modes were consistently identified for all the blades and 7 modes for the disk within the considered frequency bandwidth. Despite the presence of geometric variations among the blades (type-A, type-B, and type-C), the overall modal content remains consistent across all specimens. In particular, for a given frequency range, the same number of modes is observed, and the identified mode shapes exhibit a similar spatial distribution. The geometric differences primarily introduce small deviations in the natural frequencies. The identified natural frequencies for the disk are reported in Table 2. Since only one acquisition point per sector was considered, and measurements were performed in the out-of-plane direction, the mode shapes can be characterized only in terms of nodal diameters.

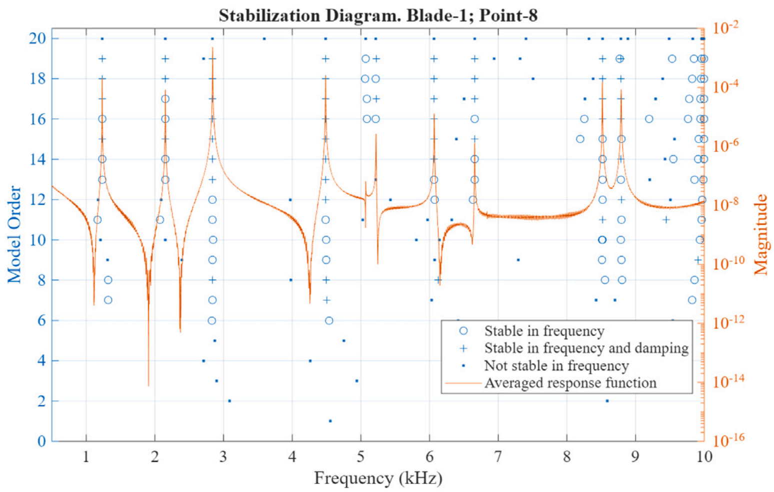

Fig. 6. Stabilization diagram obtained using the LSRF technique for a representative blade measurement point.

Table 3
Identified natural frequencies [Hz] for all blades.

Blade	M1	M2	M3	M4	M5	M6	M7	M8	M9	M10	M11
1	1231.1	2151.6	2840.1	4486.1	5068.9	5219.9	6068.3	6564.0	6837.9	8517.3	8789.9
2	1236.5	2149.3	2851.2	4355.9	4621.3	5223.2	5882.4	6735.0	7182.0	8438.1	8797.1
3	1230.9	2149.9	2832.2	4472.9	5076.7	5207.1	6072.0	6608.2	6771.0	8499.5	8774.2
4	1231.9	2149.3	2835.9	4486.5	5072.0	5215.4	6064.4	6746.0	6980.0	8521.7	8783.8
5	1233.7	2155.8	2839.6	4413.8	4656.0	5176.4	5915.1	6757.0	6736.7	8327.0	8674.0
6	1231.5	2151.0	2829.3	4608.6	5065.7	5192.5	6062.0	6558.6	6721.5	8496.2	8758.9
7	1231.5	2144.4	2826.0	4388.8	5074.6	5183.9	6073.7	6493.9	6734.4	8479.1	8740.4
8	1230.3	2143.7	2822.8	4449.9	5064.5	5192.0	6056.1	6542.3	6752.0	8516.6	8763.5
9	1231.6	2146.9	2836.5	4547.7	5122.0	5217.8	6075.1	6545.4	6826.2	8535.1	8790.8
10	1231.8	2156.2	2839.4	4506.1	5070.1	5212.3	6085.7	6715.0	6750.0	8428.0	8773.2
11	1231.0	2141.5	2822.4	4378.2	4645.7	5145.2	5907.7	6514.1	6712.9	8305.6	8629.9
12	1230.9	2150.5	2840.6	4491.8	5081.2	5212.0	6082.4	6760.0	6762.5	8490.4	8775.9
13	1234.5	2160.7	2847.7	4509.3	5071.0	5222.6	6085.4	7167.6	6785.0	8513.8	8793.7
14	1230.9	2138.6	2822.9	4410.4	5059.9	5184.4	6058.7	6416.2	6766.8	8493.5	8741.4
15	1232.1	2156.4	2839.3	4501.9	5092.2	5210.5	6084.0	6706.0	6737.9	8480.3	8776.5
16	1231.5	2135.3	2816.6	4339.2	4620.5	5141.4	5892.7	6373.2	6700.0	8295.5	8622.9
17	1232.4	2159.3	2843.7	4514.5	5062.4	5225.0	6076.2	7274.0	6821.1	8519.5	8800.9
18	1231.8	2149.4	2834.7	4466.0	5066.9	5205.5	6072.5	6571.3	6824.6	8515.0	8771.4

The identified natural frequencies for the blades are reported in Table 3. The harmonic content is consistent across all blades, as the identified frequencies are very close to each other. At the same time, the frequencies of mode 5 associated with type-A and type-B blades are lower than those of type-C blades. This mode is characterized by significant deformation in the flank region, where the presence of the fillet plays a crucial role in the local stiffness. Type-C blades, which include the fillet at the flank, exhibit higher natural frequencies due to the increased stiffness. In contrast, type-A and type-B blades, lacking this feature, present reduced stiffness and consequently lower natural frequencies.

3.2. Assembly analysis

The objective of this subsection is to investigate the dynamic behavior of the assembled bladed disk. The blades are attached to the disk by means of two bolts symmetrically positioned on both sides of the disk rim. The bolts, inserted from the disk side, press the blade root against the slot, ensuring firm contact at the blade–disk interface. For the measurements, three acquisition points are defined on the blade (at the leading edge side) and one on the disk rim. A key aspect of the assembly procedure is the selection of the tightening torque. The applied torque must be sufficiently high to guarantee proper contact and limit relative motion as well as the slipping at the interface. At the same time, excessive torque must be avoided to prevent over-stiffening and potential plastic damage of the components and threads. To determine an appropriate torque value, preliminary tests were performed on a disk–single blade assembly (Fig. 7a), considering four tightening torque levels: 5, 10, 15, and 20 Nm. Torque values above 20 Nm were observed to induce plastic deformation in the threaded connection. The identification of the assembly under these preload conditions was carried out through impact hammer testing, with excitation applied on the disk side and responses measured at the four acquisition points.

(a)

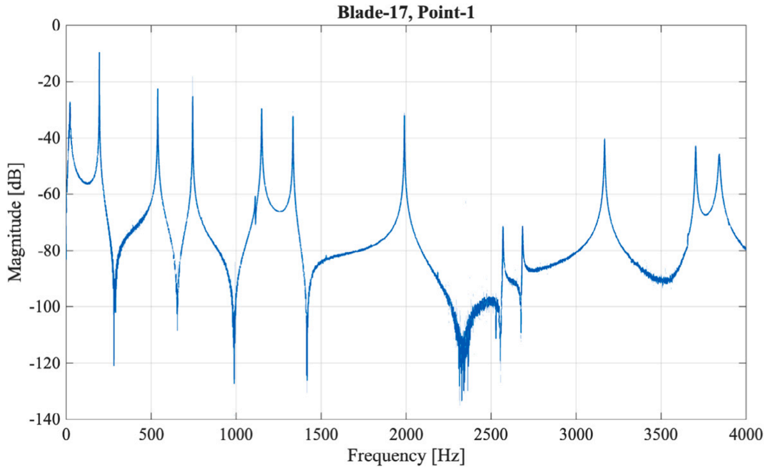

(b)

Fig. 7. Disk-one-blade assembly: (a) setup; (b) measured FRF at 20 Nm tightening torque.

An example of the measured FRF for the disk–single blade assembly is shown in Fig. 7b. The frequency bandwidth is limited to 4 kHz, above which the measurements were affected by significant noise contamination. The tests were repeated for the four selected tightening torque values, and all the measured FRFs were post-processed using the LSRF-based EMA procedure described in the previous subsection.

The variation of the natural frequencies of the first nine modes of the disk–single blade assembly as a function of the tightening torque is shown in Fig. 8. As can be observed, the increase in frequency between 5 and 10 Nm is significantly steeper compared to the variations observed between 10–15 Nm and 15–20 Nm. This indicates that a torque value of 5 Nm is insufficient to ensure firm contact at the interface, leading to partial slipping conditions. Once the contact threshold is exceeded, the frequency variation becomes more gradual and tends to stabilize. The remaining increase in frequency for higher torque values can be attributed to the local stiffening of the blade root induced by the compressive forces generated by the bolts. However, the overall sensitivity to preload remains low, with frequency variations on average in the order of approximately 0.5%. Based on these observations, a tightening torque of 20 Nm is selected for the assembly, as it ensures predominantly sticking conditions at the blade–disk interface with sufficient confidence while avoiding plastic damage.

The full bladed disk assembly is obtained by inserting each blade into its corresponding slot on the disk and securing it using two bolts positioned symmetrically at the disk rim and tightened with 20 Nm torque. The bolts, inserted from the disk side, press the blade against the bottom surface of the blade root, ensuring firm contact at the interface (Fig. 9). As a result, four main contact regions are established between the blade and the disk: the left and right sides of the blade–root interface, and the front and rear surfaces where the bolts apply pressure. The assembled system is tested under free–free boundary conditions, achieved by placing the structure on a soft elastic foam. For the measurements, three acquisition points are defined on each blade at the leading edge, and one point on the disk sector, located on the front side of the rim below each blade. In total, 72 measurement points are considered. The excitation is applied on the disk side, just above the fixture holes (Fig. 9)), and all measurements are performed in the out-of-plane direction.

An example of the measured FRF at a selected blade and measurement point of the full assembly is shown in Fig. 10(a). Due to the high modal density over the considered bandwidth, a global EMA over the full frequency range is not practical. Therefore, a local fitting strategy is adopted, where the frequency range is divided into smaller intervals. These intervals are selected such that they are sufficiently separated from adjacent modes, ensuring negligible dynamic interaction. Under this assumption, each interval can be treated as dynamically independent and analyzed separately. An example of such an interval, together with the corresponding stabilization diagram, is shown in Fig. 10(b), spanning the frequency range from 190 to 260 Hz. As can be observed from Fig. 10(a), this interval is well separated from neighboring modes, supporting the validity of the adopted assumption. In total, 82 modes were identified within the considered frequency bandwidth. The corresponding natural frequencies are graphically reported in Fig. 11.

Regarding the mode shapes, it is not practical to report all the identified modes due to space limitations. However, it can be observed that some modes exhibit characteristics similar to those of a tuned system, where the deformation follows a clear nodal diameter pattern, as shown in Fig. 12(a), corresponding to a nodal diameter of 2. In contrast, other modes are representative of the mistuned behavior, as illustrated in Fig. 12(b), where mode localization is clearly observed. In such cases, certain blades exhibit

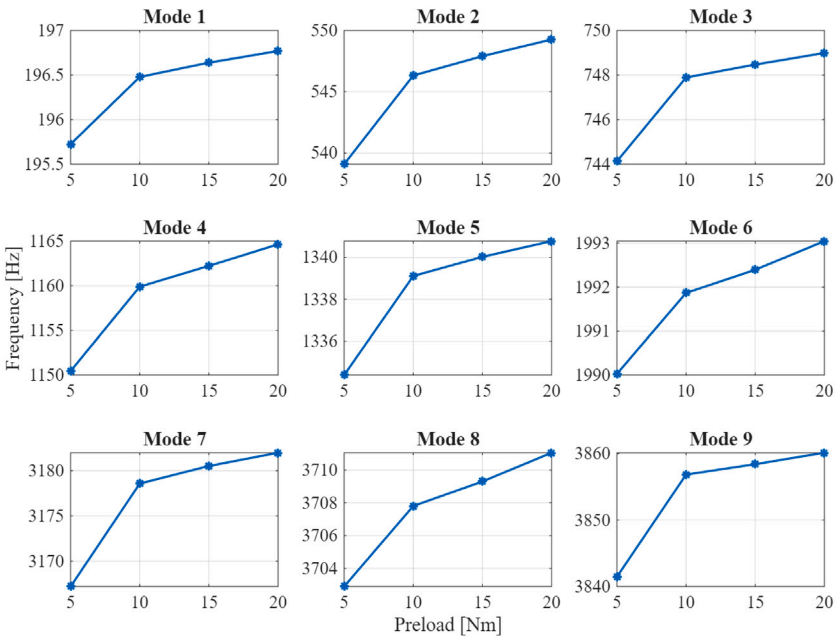

Fig. 8. Natural frequencies of the first nine modes of the disk–single blade assembly as a function of the tightening torque.

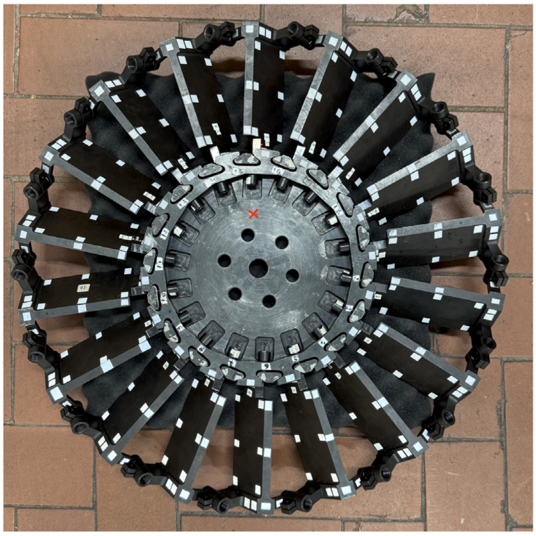

Fig. 9. Full bladed disk assembly. Red cross indicated the excitation point.

significantly higher vibration amplitudes compared to others, which is not expected in an ideally tuned configuration. In the figures, the gray markers indicate the undeformed (reference) positions of the measurement points, while the blue markers represent the displaced configuration. The brown surface corresponds to the neutral surface of the structure.

4. Numerical analysis

This section presents the numerical modeling of the bladed disk system. First, FEM of the individual components are developed. The material properties are then calibrated based on the experimental observations to ensure consistency with the measured data. The accuracy of the FEM is subsequently validated by comparison with the experimentally identified modal parameters. Following this, the assembly of the bladed disk is modeled, including the representation of the contact conditions at the blade–disk interface. ROMs are then constructed for the individual components and for the full assembly. Finally, the predictive capability of the proposed ROM framework is assessed through validation against the experimental observations.

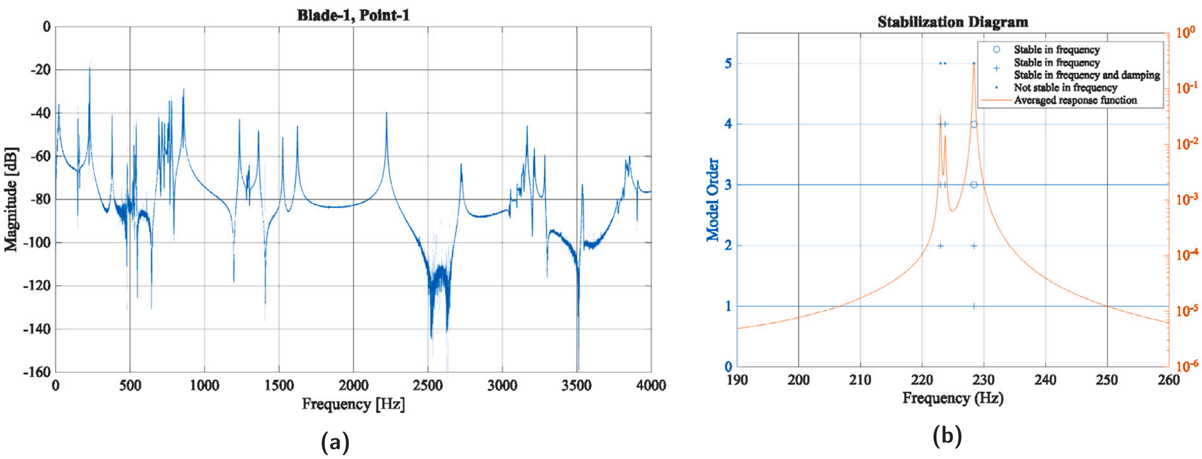

Fig. 10. (a) Example of measured FRF of the full assembly at a representative blade and measurement point; (b) corresponding stabilization diagram for a selected frequency interval (190–260 Hz).

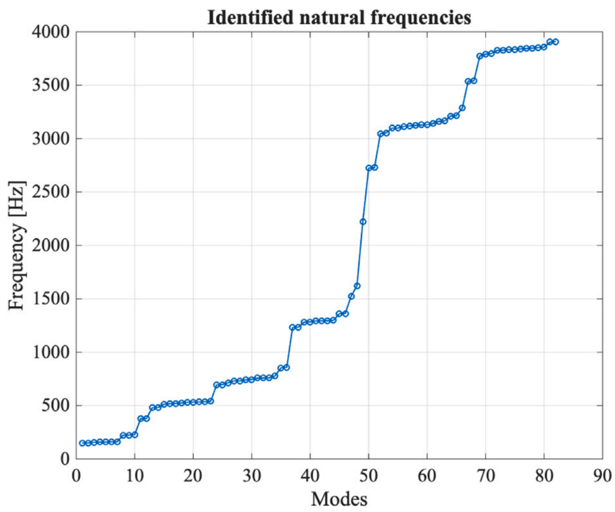

Fig. 11. Identified natural frequencies of the full assembly.

4.1. Component modeling

The numerical analysis starts with the development of the FEM of the individual components, i.e., the disk and the blade. The CAD geometries are constructed to accurately reproduce the main geometric features of the real components and are subsequently meshed using the commercially available solver ANSYS Mechanical APDL.

For the volumetric discretization, SOLID186 elements are employed. This is higher order 3-D 20-node solid element that exhibits quadratic displacement behavior. The element is defined by 20 nodes having three DOF per node: translations in the nodal x, y, and z directions. In addition, MESH200 element is used for surface meshing and for defining contact and interface regions, facilitating the implementation of assembly constraints. Particular attention is given to the meshing of the blade–disk interface, where a conforming mesh is adopted. This ensures node-to-node correspondence at the contact regions, simplifying the imposition of compatibility conditions during the assembly process.

Both components are made of the same material: quenched and tempered C40 steel (EN 10083-2, grade C40). Although three different blade geometries are present in the experimental setup (type-A, type-B, and type-C), only one representative geometry is considered for the FEM. According to Table 1, the majority of blades belong to type-C, and therefore this geometry is selected as representative. As a consequence, from a numerical standpoint, the assembled model consists of 18 identical blades. The geometric variability observed in the experimental configuration is not explicitly modeled in the FEM geometry but is instead introduced through differences in the blade natural frequencies. The final FEM of the disk and blade components are shown in Fig. 13.

The material properties of the FEM are calibrated based on experimental observations. Two main parameters are considered for tuning: the density and the Young modulus.

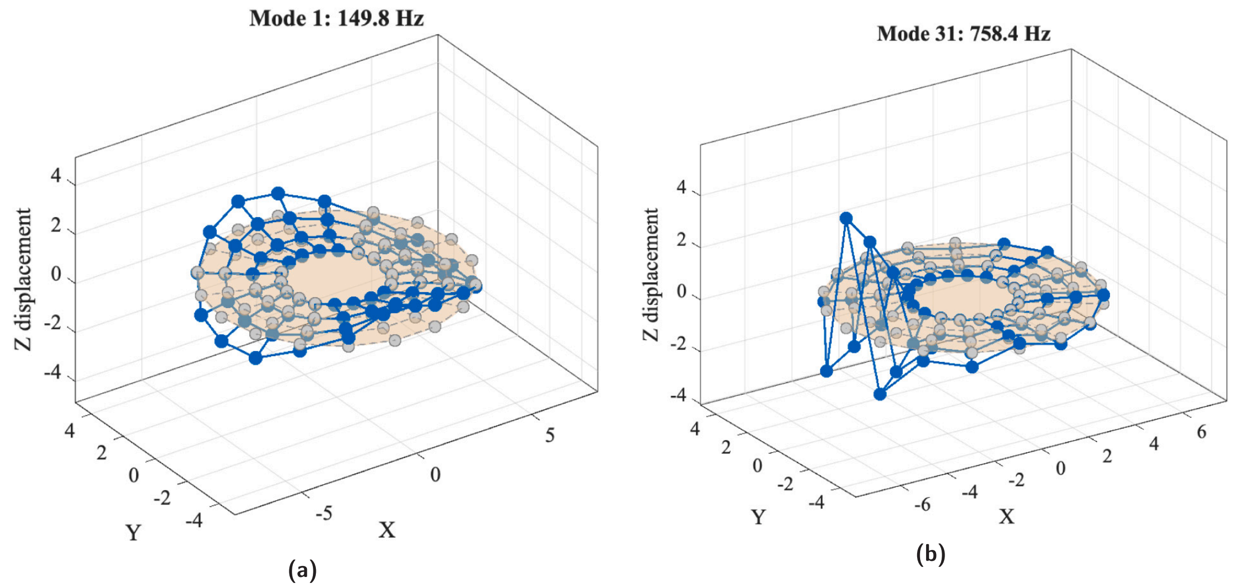

Fig. 12. (a) Mode with nodal diameter-like pattern (ND = 2); (b) localized mode due to mistuning.

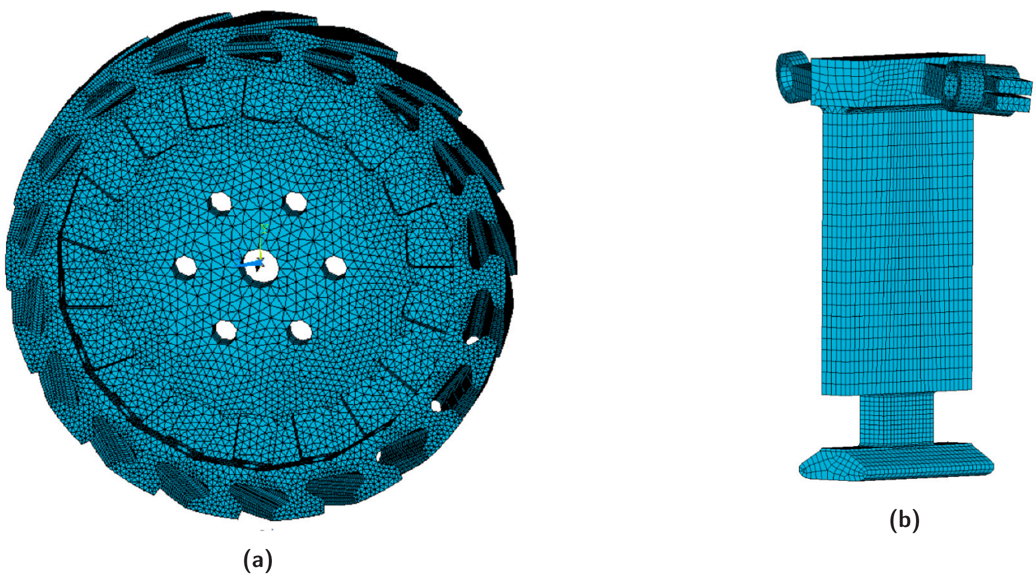

Fig. 13. FEM of the components under investigation: (a) disk; (b) blade.

The density of the disk is evaluated as a ratio of the measured mass of the actual component (Fig. 14) and the volume from the CAD model. The Young modulus is subsequently tuned by matching the first natural frequency of the FEM of the disk with the experimentally identified value, equal to 1090.6 Hz (see Table 2).

The tuning of the blade FEM follows a similar approach to that adopted for the disk component. However, since 18 blades with properties variations are present, the calibration of a single representative model requires additional considerations. All the blades are found to have the same mass, equal to 240 g with a scale having a precision of ±5 g. The density is therefore the ratio of the mass and a volume of the CAD model. The Young modulus of the blade is calibrated such that the mean value of the squared natural frequencies (i.e., the mean eigenvalue) of the first mode of all blades (see second column of Table 3) matches the squared natural frequency of the first mode of the corresponding FEM. This choice is motivated by the fact that the perturbations later introduced in the eigenvalue matrix of the blade ROM (see Eq. (20)) are considered to have zero mean for the first mode. As a result, this approach ensures a consistent representation of the average stiffness of the blade population and avoids introducing a systematic bias in the model. The calibrated values of the density and Young modulus for both the blade and disk are summarized in Table 4

Fig. 14. Disk component weighted on scale.

Table 4
Calibrated material parameters of the components.

Component	Density [kg/m^3]	Young Modulus [GPa]
DISK	7864.6	202
BLADE	7832.5	212

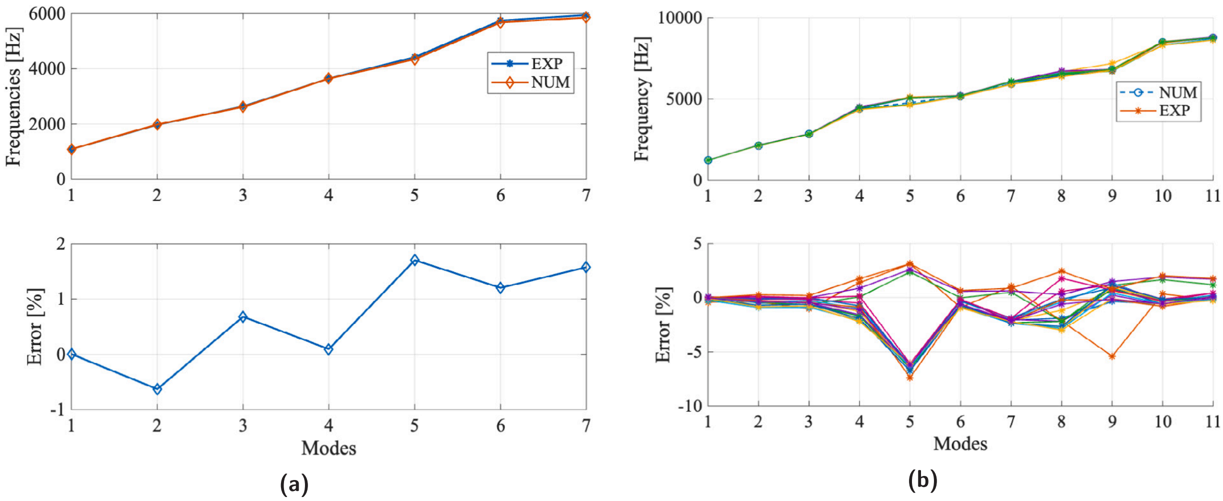

Fig. 15. (a) Validation of the disk FEM; (b) validation of the blade FEM through comparison of natural frequencies.

Fig. 15(a) shows the validation of the disk FEM by comparing the natural frequencies obtained from the tuned numerical model with the experimental results (see Fig. 15). Very good agreement is observed, with errors remaining below 2% for all identified modes. Fig. 15(b) presents the validation of the blade FEM. Due to space limitations, legends are reported; in the upper plot, dashed lines correspond to numerical results, while solid lines represent the experimental frequencies of the 18 blades. Overall, a good agreement is observed across all modes.

A slightly larger discrepancy is observed for mode 5. As discussed in Section 3.1, this mode is characterized by deformation concentrated at the top flank, where the presence of the fillet strongly influences the local stiffness. In the FEM, the fillet geometry is slightly simplified to avoid excessively refined and impractical mesh regions. As a result, the stiffness of this region is slightly underestimated, leading to lower predicted natural frequencies compared to the experimental type-C blades, while remaining higher than those of type-A and type-B blades, where the fillet is absent.

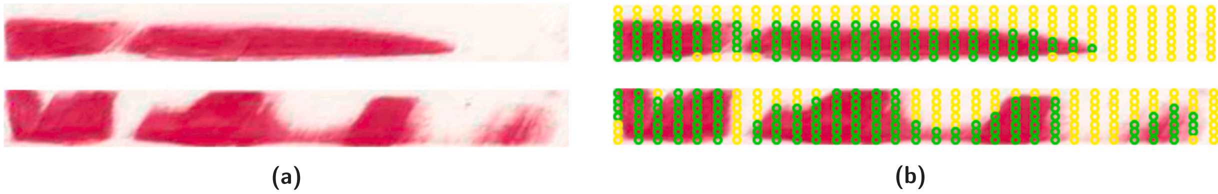

Fig. 16. (a) Pressure film contact pattern at blade–root joint; (b) extracted contact nodes from image processing (green circles: contact; yellow circles: no contact).

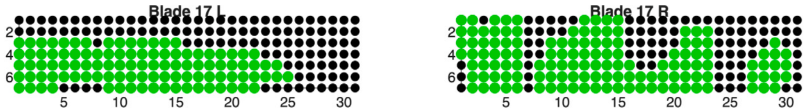

Fig. 17. The resulting contact grid after the image post-processing.

4.2. Contact modeling and system assembly

Before assembling the full system, the modeling of the contact at the blade–disk interface must be addressed. Several approaches can be adopted, including penalty-based contact formulations, nonlinear frictional contact models, or simplified compatibility-based approaches. In the present study, a linear analysis framework is considered, focusing on the identification of natural frequencies and mode shapes. Moreover, the experimental conditions correspond to impact hammer testing with small vibration amplitudes and a relatively high tightening torque of 20 Nm, ensuring firm contact at the interface. Under these conditions, the effects of contact nonlinearity and friction are expected to be negligible. Therefore, a simplified contact modeling approach is adopted, where node-to-node compatibility conditions are enforced at the interface. This corresponds to a direct coupling of the DOF of the contacting nodes, ensuring displacement continuity without introducing additional contact elements or nonlinearities. Therefore, the nodes located at the coincident regions of the blade and disk components are considered for the assembly. In the ideal case, all interface nodes are assumed to be in contact, and compatibility conditions are imposed on the entire contact surface. However, as shown in the authors' previous work [35,36], this assumption does not hold in practice. Due to manufacturing tolerances and surface roughness, only a portion of the nominal contact surface is effectively in contact. This phenomenon is referred to as contact mistuning. Moreover, previous studies [43,44] demonstrated that variations in the blade–disk contact topology produce measurable changes in the modal characteristics of the assembled bladed disk. Therefore, the experimentally identified contact maps are incorporated into the present formulation to account for this additional source of mistuning.

In the same study, an experimental campaign was conducted by inserting a pressure-sensitive film at the blade–disk interface of the same bladed disk configuration. A tightening torque of 20 Nm was applied, and the resulting colored regions on the film were used to identify the actual contact areas, while the non-colored regions correspond to detached zones. This effect was consistently observed across all 18 blade–disk joints. Due to the repeatability of the manufacturing process, the contact patterns exhibit a certain degree of similarity. In particular, the patterns corresponding to the low side of the joint are similar among themselves, as are those corresponding to the high side. An example of a contact pattern obtained from a pressure film at the blade–root interface of blade 17 is shown in Fig. 16a, where top figure shows the pattern on the low side and bottom one the pattern on the high side.

To translate this pattern into a set of contacting nodes for the FEM, an image processing procedure is applied. The contact interface in our FEM is discretized by a regular grid of nodes arranged in a 7×31 layout. This grid is superimposed onto the pressure film image, as illustrated by the green and yellow circles in Fig. 16(b). A threshold on the color intensity is then defined to distinguish between contact and non-contact regions. If the intensity at a given grid point exceeds the threshold, the corresponding node is considered to be in contact; otherwise, it is treated as detached. In Fig. 16(b), nodes identified as being in contact are marked with green circles, while yellow circles denote non-contacting node. The resulting contact grid at the same blade-root joint is illustrated in Fig. 17. The resulting contact grid applied to the FEM is illustrated in Fig. 18(a) and (b), corresponding to the low and high sides of the blade–disk interface, respectively.

Before performing the validation of the disk–single blade assembly with the implemented contact grid, a minor modification is introduced in the FEM to account for the presence of the tightening bolts. Specifically, the bolts are modeled as additional components with the same geometry and are positioned at the fixture locations (see Fig. 18b). This approach allows for a more accurate representation of the mass contribution of the bolts compared to a simplified lumped mass assumption, for which the exact position of the center of mass would be difficult to determine. Another contact region, i.e., the interface between the blade and the bolt, along which the preload is transmitted to secure the blade within the disk slot, is also modeled. In this case, a simple node coupling approach is adopted by enforcing compatibility conditions at the corresponding nodes.

The validation of the disk–single blade assembly in the presence of contact mistuning is performed by comparing the natural frequencies (Fig. 19(a)) and the mode shapes (Fig. 19(b)). As shown in Fig. 19(a), an excellent agreement is observed between the numerical and experimental natural frequencies across all identified modes. The deviations remain small, with a mean absolute

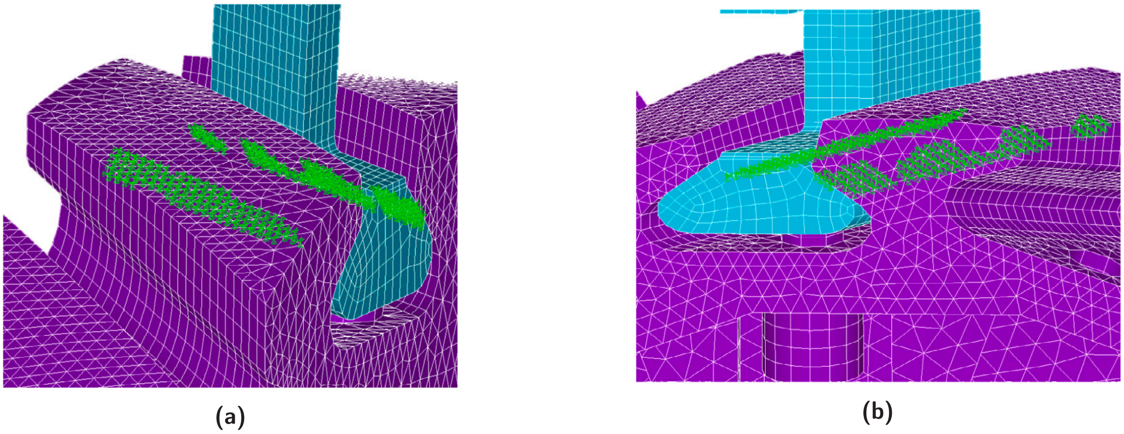

Fig. 18. Contact nodes applied to the FEM: (a) low side; (b) high side of the blade–disk interface.

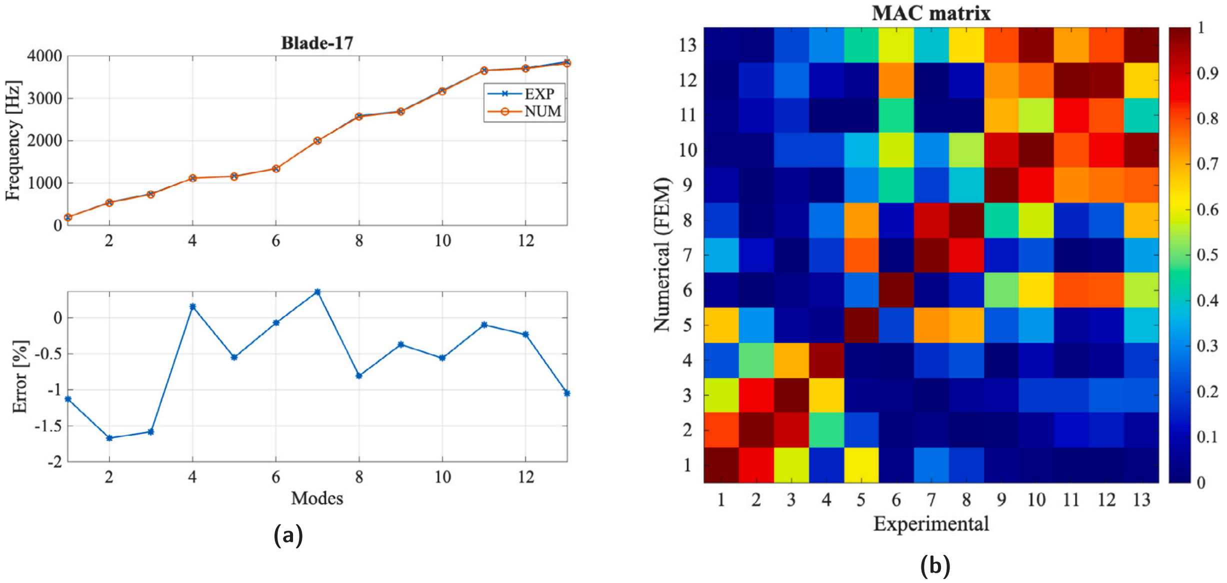

Fig. 19. Validation of the disk–single blade assembly: (a) natural frequencies comparison; (b) MAC matrix between numerical and experimental mode shapes.

error of 0.66% over the 13 identified modes. The comparison of mode shapes, reported through the MAC matrix in Fig. 19(b), further confirms the accuracy of the model. The diagonal terms indicate a clear one-to-one correspondence between numerical and experimental modes, with high MAC values, which are close to one. The results presented in Fig. 19 refer to the assembly with blade 17. Although similar results can be obtained for all blade configurations, only one representative case is shown here for clarity. It is worth noting that all blade assemblies exhibit comparable levels of accuracy, both in terms of natural frequency errors and MAC values.

4.3. Reduced-order model

The next step consists in constructing ROM of the individual components, i.e., the disk and the blade, treated as substructures. The disk component is reduced using the Craig–Bampton fixed-interface reduction technique (see Section 2.1), while the blade component is reduced using the Rubin free-interface reduction method (see Section 2.2). The latter is adopted to enable the introduction of mistuning through perturbations of the free-interface natural frequencies, which represents a key aspect of the proposed framework. For the disk, 300 fixed-interface modes are retained, whereas for the blade, 50 free-interface modes are considered. These values are selected as a trade-off between the accuracy of the ROM and the size of the substructures. The Craig–Bampton method typically provides higher accuracy for lower-frequency modes, which justifies retaining a larger number of modes

Table 5
DOFs of the FEM prior to reduction.

Component	DOFs
Disk — excess	2,177,277
Disk — disk–blade interface (per slot)	1302
Disk — bolt–blade interface (per slot)	306
Disk — accessory	54
Disk — total	**2,206,275**
Blade — excess	229,989
Blade — blade–disk interface	1302
Blade — blade–bolt interface	306
Blade — accessory	9
Blade — total	**231,606**

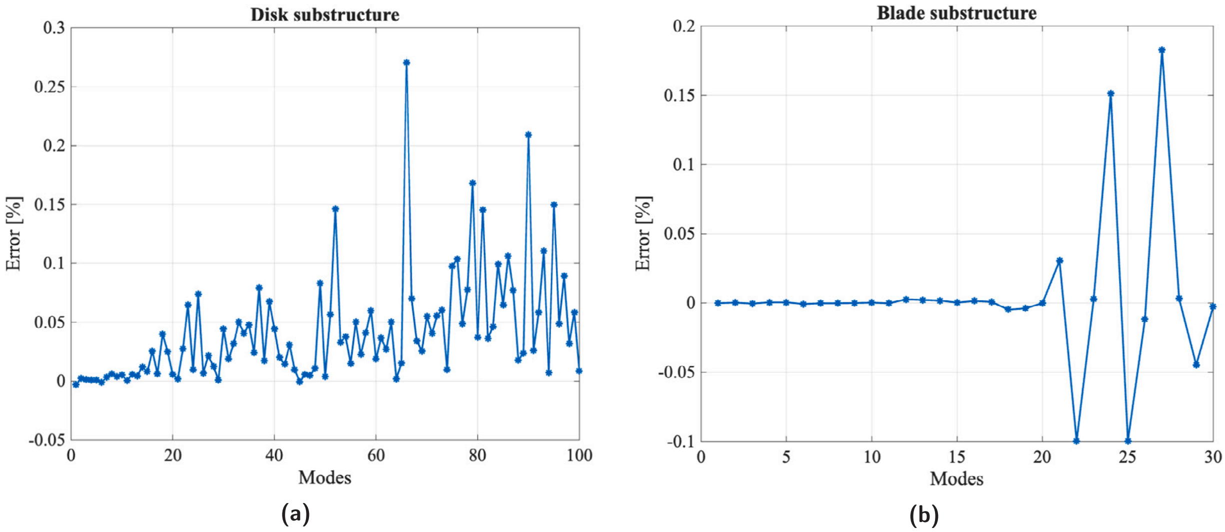

Fig. 20. Validation of ROMs: (a) disk substructure; (b) blade substructure (relative error in natural frequencies).

for the disk [29]. In contrast, the Rubin free-interface reduction exhibits a more uniform approximation accuracy across the retained modes and increasing the number of retained modes did not provide a noticeable improvement in accuracy. Moreover, the full assembly consists of one disk and 18 blade substructures, which further supports limiting the number of retained blade modes to control the overall system size.

The retained boundary DOFs, corresponding to the master DOFs (see Eq. (4)), are selected based on the physical interfaces and measurement locations. For the disk, these include the contact interface DOFs at the blade–disk and bolt–blade interfaces for each slot, as well as one additional measurement node per sector, resulting in a total of 18 measurement DOFs. For the blade, the retained DOFs correspond to the same interface nodes, along with three additional measurement nodes used in the experimental campaign. The sizes of the FEM prior to reduction are illustrated in Table 5. The reduction process results in significant compression, with a reduction of 99.3% for the blade model and 98.6% for the disk model sizes.

The accuracy of the ROM is assessed by comparing the natural frequencies of the substructures obtained from the ROM with those of the corresponding full FEM, for both the disk (Fig. 20(a)) and the blade (Fig. 20(b)). As shown in Fig. 20(a), the ROM of the disk substructure exhibits an excellent agreement with the full FEM over the considered modes. The relative error remains very low, generally below 0.3%, indicating that the selected number of fixed-interface modes ensures a highly accurate representation of the disk dynamics.

Similarly, the blade ROM demonstrates a very good agreement with the FEM, as illustrated in Fig. 20(b). The errors remain negligible for most of the retained modes, with slightly larger deviations observed only at higher modes, where the approximation becomes more sensitive. Nevertheless, the overall accuracy remains high, confirming that the chosen number of free-interface modes is sufficient to capture the dynamic behavior of the blade. These results validate the effectiveness of the adopted reduction strategies for both substructures and confirm their suitability for the subsequent assembly and mistuning analysis.

The full tuned bladed disk assembly is then validated in the absence of both blade and contact mistuning. The validation is performed by comparing the first 100 natural frequencies obtained from the ROM with those of the full FEM. In addition, the corresponding mode shapes are compared by means of the MAC, considering four DOFs per sector, resulting in a total of 72 DOFs for the full assembly. As shown in Fig. 21(b), the MAC values are close to unity for the majority of the modes, typically exceeding 0.98 and remaining above 0.95 in most cases, indicating an excellent correlation between the ROM and FE mode shapes, with only

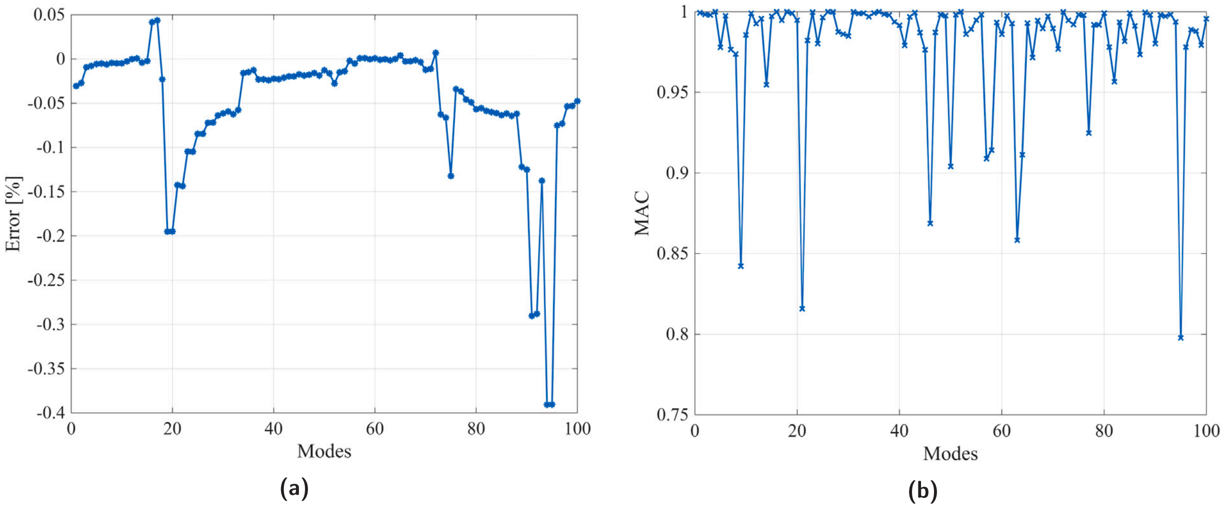

Fig. 21. Validation of ROM of the tuned bladed disk: (a) natural frequency difference; (b) diagonal values of the MAC matrix.

a few localized reductions reaching values around 0.80–0.85. The standard matrix representation of the MAC is omitted due to the large number of modes, which would make the matrix visualization unclear and difficult to interpret. The frequency errors, reported in Fig. 21(a), remain very small overall, generally within $\pm 0.05\%$, with slightly larger deviations observed only for a limited number of modes, where the error can reach approximately -0.35%.

The next step consists in constructing the ROM of the bladed disk, accounting for both blade and contact mistuning. The contact mistuning is introduced through the experimentally derived contact grids for each blade–disk interface (see Section 4.2), obtained from pressure-sensitive film measurements. In contrast, blade mistuning is modeled by perturbing the free-interface eigenvalue matrix appearing in the reduced stiffness matrix of the blade component (see Eq. (20)). This formulation provides a high level of flexibility, as it allows independent perturbation of each retained mode for each blade. In the present work, the perturbations are derived directly from experimental measurements of the individual blades (Table 3). Specifically, the perturbation coefficients are computed as

$$\delta_i^{(j)} = \frac{\left(\omega_{f,i}^{(j)}\right)^2 - \omega_{f,i}^2}{\omega_{f,i}^2}, \tag{27}$$

where $\omega_{f,i}$ denotes the ith free-interface natural frequency of the tuned blade (ROM), while $\omega_{f,i}^{(j)}$ corresponds to the experimentally identified natural frequency of the jth blade. The resulting perturbations are illustrated in Fig. 22. Figure shows the eigenvalue perturbations for all 18 blades. For clarity, individual legends are omitted; however, the figure provides an overview of the spread and variability of the perturbations across the modes. As can be observed, the magnitude of the perturbations is not negligible, indicating a noticeable level of mistuning. This leads to a challenging validation scenario for the proposed modeling framework. The number of perturbed modes corresponds to the number of experimentally identified modes, while the remaining higher modes are left unperturbed (tuned). As a result, 18 distinct blade substructures are obtained, each characterized by its own perturbed eigenvalue matrix, such that the corresponding natural frequencies match those of the real blades. It is important to note that the underlying FEM is based on a single representative geometry (type-C blade), while the actual blades exhibit both intrinsic and geometric mistuning. Therefore, the geometric variability is implicitly introduced into the model through the experimentally identified natural frequencies, further increasing the severity of the mistuning conditions. Finally, the assembly of the full system is carried out by enforcing compatibility conditions at the blade–disk and bolt–blade interfaces through node coupling, while incorporating the contact mistuning patterns described earlier.

Fig. 23(a) shows the first 100 natural frequencies of the mistuned ROM, compared with those of the corresponding tuned system, where both blade and contact mistuning are not considered. As observed, the overall trend of the frequency distribution remains similar, with only moderate deviations introduced by mistuning. The lower plot highlights the relative differences between the two cases, which remain generally small and reach values up to approximately 3% for some modes. This confirms that mistuning has a limited influence on the natural frequencies.

However, the most significant effect of mistuning is observed in the mode shapes. Fig. 23(b) reports the diagonal values of the MAC matrix between the mode shapes of the mistuned ROM and those of the tuned model for the first 100 modes. A strong variability of the MAC values can be observed, with several modes exhibiting low correlation, indicating substantial differences in mode shapes. This behavior is characteristic of mistuned systems, where mode localization may occur, leading to vibration energy being concentrated on a limited number of blades. The dashed line in Fig. 23(b) represents the mean MAC value, which remains relatively low, further emphasizing the global discrepancy between the tuned and mistuned mode shapes. These results clearly

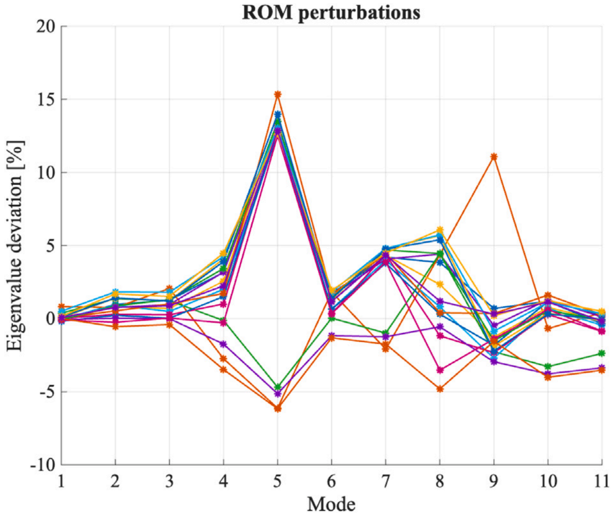

Fig. 22. Eigenvalue perturbations used to introduce blade mistuning in the ROM.

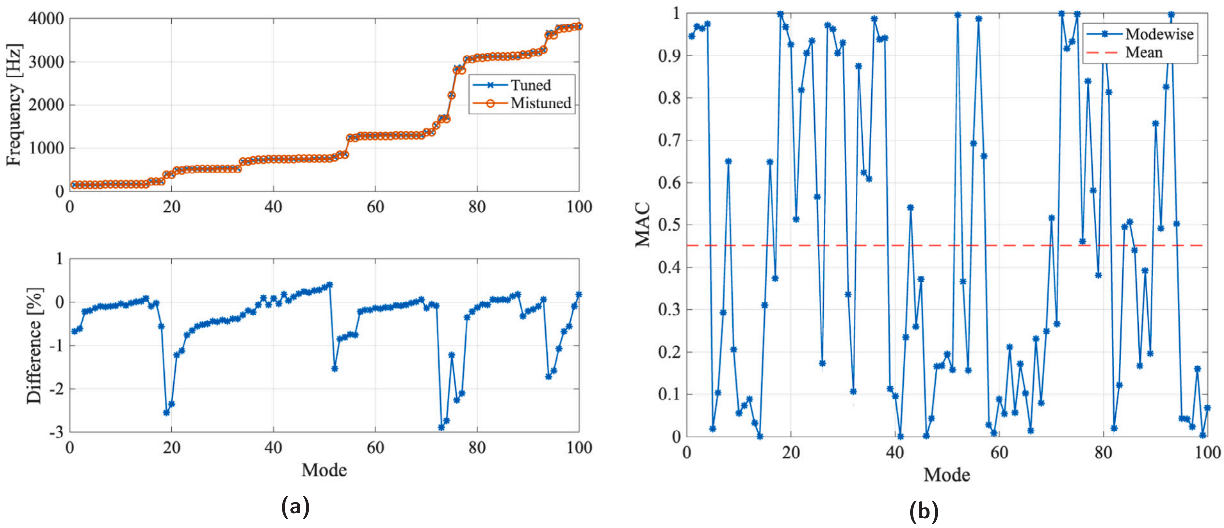

Fig. 23. (a) Natural frequencies of tuned and mistuned ROM and their relative difference; (b) MAC between tuned and mistuned mode shapes.

demonstrate that the mistuning has a pronounced impact on the mode shapes, making their accurate prediction essential for reliable dynamic analysis.

5. Results and discussion

This section presents the results obtained from the mistuned ROM, which incorporates both blade and contact mistuning, and compares them with the experimental observations. A key preliminary step in the validation process is the identification of the correspondence between numerical and experimentally identified modes. In ideally tuned bladed disks, the cyclic symmetry leads to the formation of modal families, where groups of modes share similar spatial characteristics and are associated with specific nodal diameters. Within each modal family, modes are closely spaced in frequency, resulting in a high modal density over relatively narrow frequency bands.

Although mistuning breaks the cyclic symmetry and the concept of modal families, the overall structure of high modal density is largely preserved (see Fig. 11). As a result, several modes remain clustered within small frequency intervals, making the mapping between numerical and experimental modes based solely on natural frequencies unreliable. This difficulty is further compounded by the experimental identification process: due to the very high modal density (often 10–15 modes within a few Hertz), some modes cannot be clearly resolved and may remain unidentified. Consequently, a simple one-to-one mapping based on frequency ordering is not appropriate.

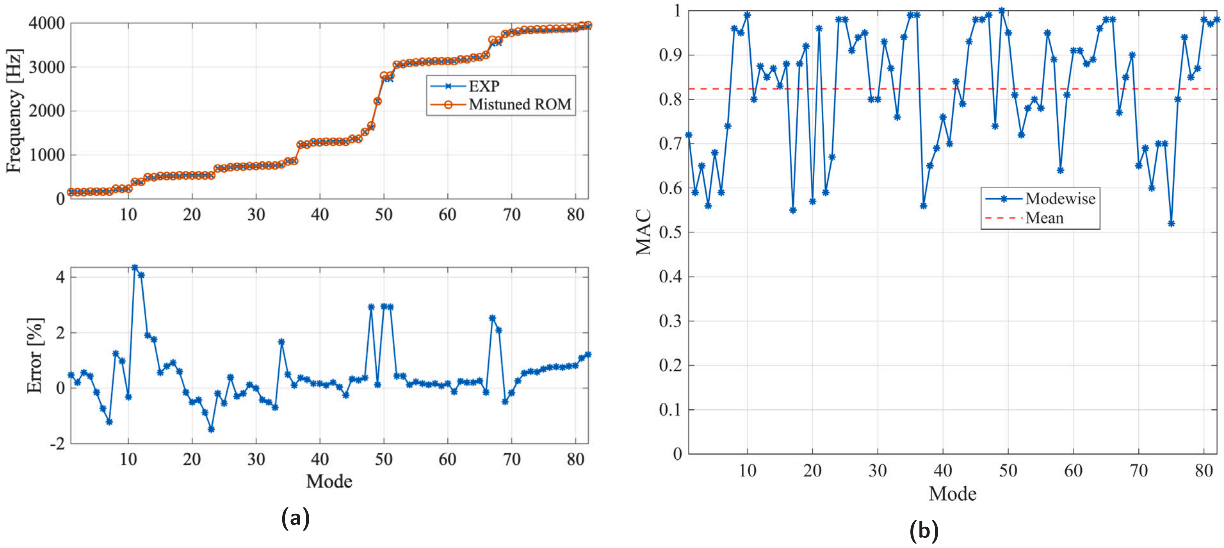

Fig. 24. (a) Comparison of natural frequencies between experiment and mistuned ROM and corresponding error; (b) MAC between experimental and numerical mode shapes.

To address this issue, a correspondence between numerical and experimental modes is established based on the similarity of their spatial distributions. For each experimentally identified mode, a set of candidate numerical modes is selected within a frequency neighborhood around the experimental value. The MAC is then evaluated between the experimental mode shape and each candidate numerical mode. Since mode shapes associated with different modes exhibit distinct spatial patterns, only one numerical mode yields a high MAC value with the experimental mode, while the remaining candidates show low correlation. This allows for an unambiguous identification of the corresponding numerical mode.

As discussed in Section 3.2, a total of 82 modes were identified from the experimental data. During the mapping procedure, these modes were successfully associated with the first 103 numerical modes, indicating a good level of agreement between the experimental and numerical models. The remaining modes could not be identified experimentally for two main reasons. First, the high modal density, combined with measurement noise, limits the capability of the LSRF technique to accurately separate closely spaced modes. In several frequency bands, multiple modes are located within a very narrow interval, making their individual identification challenging. Second, some modes exhibit dominant motion in directions that are not aligned with the measurement direction. Since the experimental acquisition is limited to a specific DOF, these modes may have a very low observable response in the measured FRFs. As a result, their corresponding peaks can be masked by noise, making their identification difficult or, in some cases, practically impossible.

The final validation is performed by comparing the natural frequencies and mode shapes of the mistuned ROM with the experimental observations. It should be emphasized that both numerical and experimental mode shapes consist of 72 DOFs, corresponding to 4 DOFs per sector (three on the blade and one on the disk sector). This represents a particularly stringent validation condition, since, unlike common practice where a single DOF per sector is considered to capture only the spatial distribution qualitatively, the present approach employs multiple DOFs per sector to achieve not only a qualitative but also a quantitative description of the mode shapes, enabling a more detailed characterization of the spatial distribution and localization patterns.

Fig. 24(a) presents the comparison of natural frequencies, where the upper plot shows the direct comparison between experimental and numerical values, while the lower plot reports the relative error. An overall very good agreement can be observed between the mistuned ROM and the experimental results. The predicted frequencies closely follow the experimental trend across the entire spectrum, demonstrating the capability of the proposed model to accurately capture the global dynamic behavior of the system. The relative error remains generally low, mostly within $\pm 1\%$, with slightly higher deviations observed only in limited regions, reaching values up to approximately 4%. These discrepancies can be attributed to the combined effects of high modal density, measurement uncertainties, and the approximations introduced in the modeling of contact and geometric variability. Nevertheless, the overall accuracy confirms the effectiveness of the proposed mistuning modeling strategy.

Fig. 24(b) shows the diagonal values of the MAC matrix between the numerical and experimental mode shapes. The MAC values remain consistently high for the majority of the modes, often exceeding 0.8, always staying above 0.5 and approaching unity for several cases, indicating a strong correlation between predicted and measured mode shapes. Some localized reductions in MAC can be observed, which are mainly associated with modes characterized by strong localization, closely spaced frequencies, or measurement uncertainties, where small discrepancies in mode identification may occur. It was additionally verified from the experimental measurements that the modes exhibiting lower MAC values are generally associated with a lower signal-to-noise ratio at the measurement points compared to modes with higher MAC values. This behavior is related to the lower mobility of these

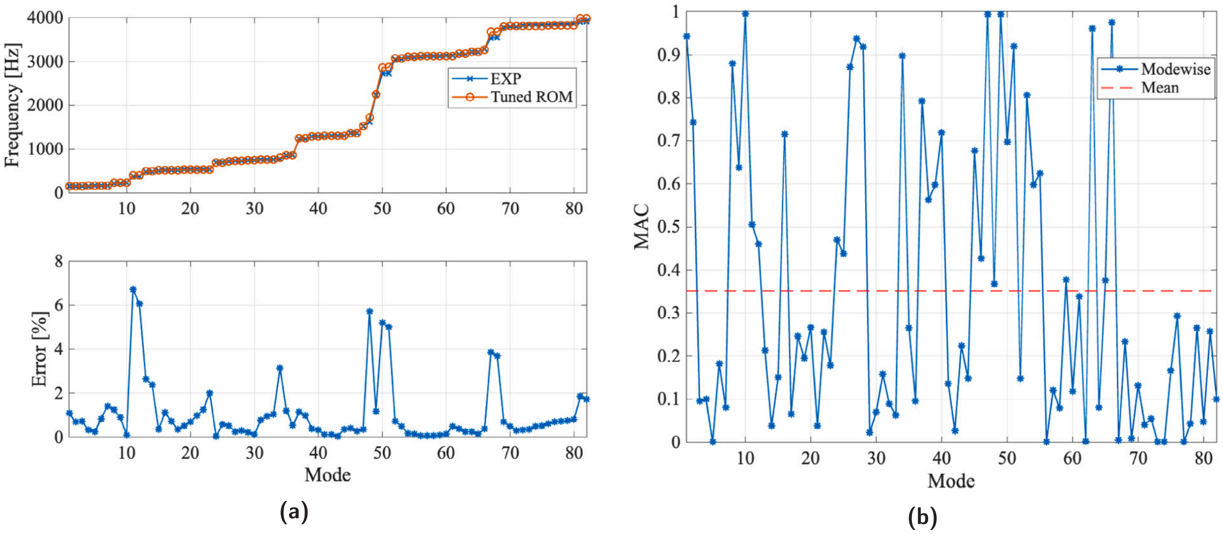

Fig. 25. Tuned ROM: (a) natural frequencies and error; (b) MAC with experimental mode shapes.

Table 6
Comparison of mean performance metrics for tuned and mistuned ROMs.

	Mean absolute frequency error [%]	Mean MAC
Mistuned ROM	0.72	0.82
Tuned ROM	1.05	0.35

points in the measurement direction, indicating that the observed MAC reductions are influenced not only by the ROM accuracy but also by the quality of the experimental measurements themselves. The dashed line represents the mean MAC value, which remains high, further confirming the overall quality of the mode shape prediction.

In order to better highlight the effectiveness of the proposed approach, the same comparison is repeated using a tuned ROM, where neither blade nor contact mistuning is taken into account. The results are shown in Fig. 25.

Fig. 25(a) compares the natural frequencies of the tuned ROM with the experimental results. Although the general trend of the frequency distribution is captured, larger discrepancies can be observed compared to the mistuned ROM. The error plot shows that deviations can reach values up to approximately 6%–7% for certain modes, with several frequency bands exhibiting systematic mismatches. This behavior indicates that the tuned assumption is less effective to accurately reproduce the dynamics of the real system, where mistuning effects are inherently present.

An even more pronounced difference is observed in the mode shapes, as shown in Fig. 25(b), where the MAC values between the tuned ROM and experimental mode shapes are reported. The MAC values are generally low and highly scattered, with many modes showing very poor correlation. The mean MAC value is significantly lower compared to the mistuned ROM case, indicating that the tuned model fails to capture the actual spatial characteristics of the vibration modes.

By comparing these results with those obtained from the mistuned ROM (Fig. 24), it becomes evident that the inclusion of both blade and contact mistuning is essential for an accurate prediction of the system dynamics. While the tuned model may provide a rough estimation of the frequency distribution, it is not capable of reproducing the correct mode shapes and leads to significantly larger errors. In contrast, the proposed mistuned ROM demonstrates a substantial improvement in both natural frequency prediction and mode shape correlation, confirming the importance and effectiveness of the adopted modeling strategy.

Since a total of 82 modes are analyzed, a concise and representative assessment of the results is provided in terms of mean values. Table 6 reports the mean absolute frequency error (note that, unlike Figs. 24 and 25, absolute values are considered) and the mean MAC for both the mistuned and tuned ROMs. As can be observed, the mistuned ROM achieves a lower mean absolute frequency error (0.72%) compared to the tuned ROM (1.05%), confirming the improved accuracy in predicting the natural frequencies. The mistuned ROM achieves a higher mean MAC value (0.82) compared to the tuned ROM (0.35), indicating a significantly improved correlation in mode shapes.

To further investigate the predictive capability of the mistuned ROM, a set of modes are examined in more detail, namely modes 1, 31, 80, and 75. As discussed in Section 3.2, a mistuned bladed disk may exhibit two different types of modal behavior. Some modes still retain characteristics similar to those of an ideally tuned system, showing recognizable nodal diameter patterns. These modes are typically well separated in frequency from neighboring modes, such that the modal participation of adjacent modes in their response remains negligible. Others are intrinsic to mistuned configurations and are characterized by mode localization, where the vibration amplitude is concentrated on a limited number of blades. In contrast to the previous case, these modes are located in

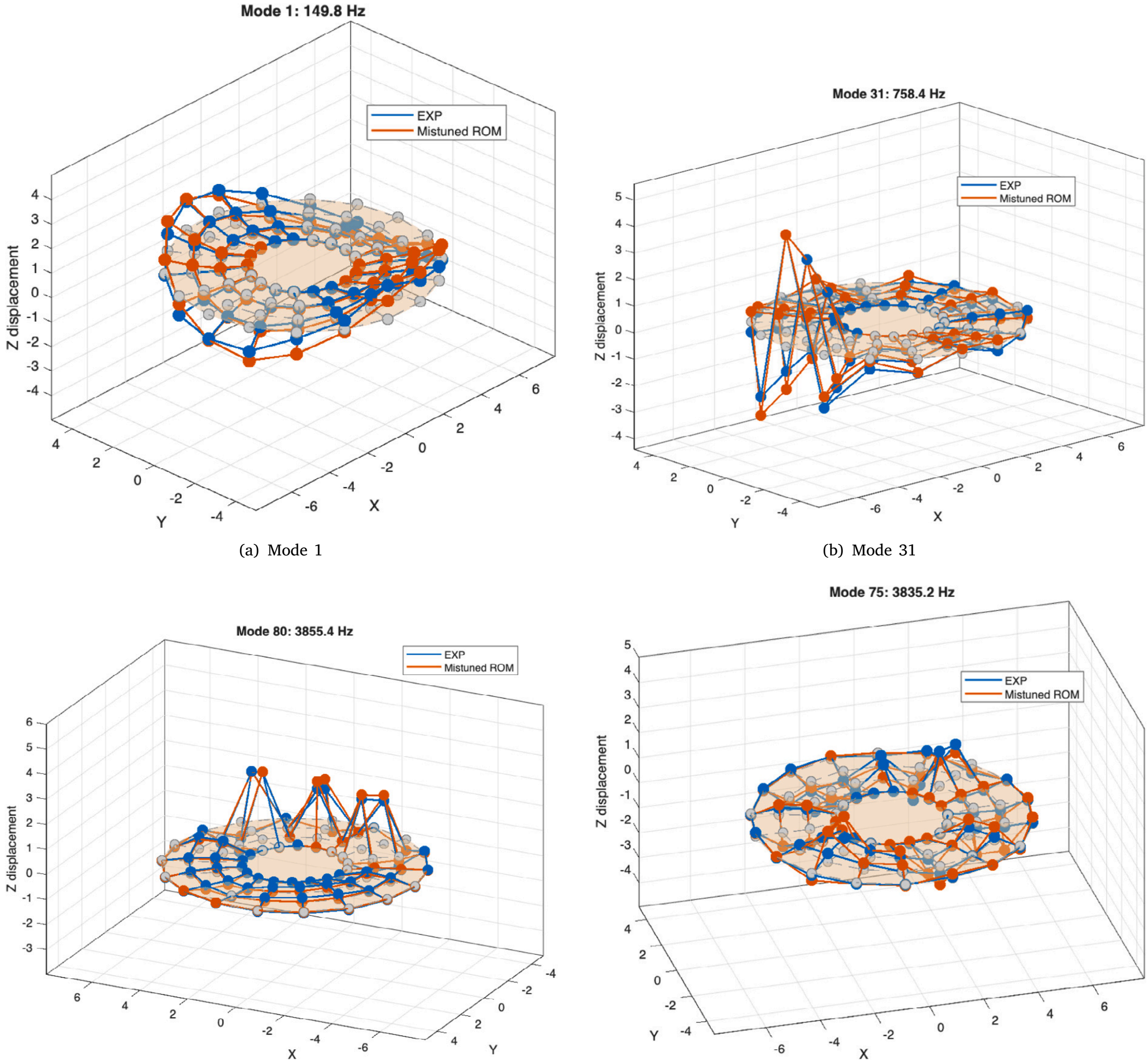

(a) Mode 1 (b) Mode 31

(c) Mode 80 (d) Mode 75

Fig. 26. Comparison between experimental and mistuned ROM mode shapes for selected modes.

Table 7
Summary of selected modes used for detailed comparison between experiment and mistuned ROM.

Mode	Experimental frequency [Hz]	Absolute frequency error [%]	MAC
Mode 1	149.8	0.47	0.72
Mode 31	758.4	0.41	0.93
Mode 80	3855.4	0.81	0.98
Mode 75	3835.2	0.68	0.52

a frequency region with high modal density. The objective of this analysis is to verify whether the proposed mistuned ROM is able to reproduce both types of behavior. A summary of the selected modes is reported in Table 7.

Fig. 26(a) compares the experimental and numerical mode shapes for mode 1. This mode is representative of a tuned-like behavior, with a clear nodal diameter pattern equal to 2. The obtained MAC value is 0.72, indicating a satisfactory agreement. The mistuned ROM is therefore able to reproduce this global pattern correctly. It is worth noting that this type of mode can also be reasonably captured by a tuned model, since the effect of mistuning on the spatial distribution is limited.

Figs. 26(b) and 26(c) show two localized mode shapes, corresponding to modes 31 and 80. These modes are particularly important, since localization is one of the main characteristics of mistuned systems and cannot be reproduced by an ideally tuned model. In both cases, the mistuned ROM provides an excellent prediction of the experimental mode shapes, with MAC values equal to 0.93 and 0.98, respectively. The agreement is evident not only in terms of the blade exhibiting the maximum mobility, but also in the overall spatial distribution of the response. For comparison, the tuned ROM yields much lower MAC values for the same modes, equal to 0.15 and 0.04 (Fig. 25), confirming that a tuned formulation is unable to capture localized behavior.

Finally, the worst predicted case is also examined, corresponding to mode 75 (see Fig. 24), shown in Fig. 26(d). This mode yields the lowest MAC value among the investigated cases, equal to 0.52. Although the agreement is less accurate compared to the other examples, the mistuned ROM still reproduces the general spatial trend of the mode shape. In particular, the blade exhibiting the maximum displacement is correctly identified, meaning that the model is still able to capture the dominant localization feature of the response. This observation is important, since even in the least favorable case the proposed approach preserves the essential dynamic characteristics of the experimental mode shape. It is worth noting as well that this mode exhibits a complex spatial pattern, which makes its accurate prediction more challenging and explains the lower MAC value observed.

6. Conclusion

This work presented an experimentally validated ROM framework for mistuned bladed disks, referred to as the Free-Interface Blade Mistuning (FIBM) method. The proposed approach combines a Rubin free-interface reduction for the blade component with a Craig–Bampton reduction for the disk sector, so that blade mistuning can be introduced directly through perturbations of experimentally measurable free-interface natural frequencies. In this way, the formulation preserves a clear physical interpretation of the reduced coordinates and provides a direct link between experimental observations and the numerical model. The methodology also incorporates contact mistuning at the blade–disk interface through experimentally derived contact patterns, enabling the simultaneous representation of intrinsic and contact-induced variability within a unified reduced-order framework.

An extensive experimental campaign was carried out to characterize both the individual components and the assembled system. Free–free modal testing of the disk and the 18 dummy blades made it possible to identify the component natural frequencies and mode shapes, while also revealing the presence of blade-to-blade variability associated not only with manufacturing tolerances but also with geometric differences among the blades. The assembled bladed disk was then tested under a controlled bolt preload condition, allowing the extraction of a large set of experimental modes for subsequent validation. In total, 82 modes were identified experimentally within the considered bandwidth, providing a particularly demanding validation basis for the numerical model.

On the numerical side, the FEM of the disk and blade components were calibrated against experimental data through tuning of the density and Young modulus, and subsequently reduced using the proposed component-level strategy. The ROM of the individual substructures showed excellent agreement with the corresponding full FEM, confirming the accuracy of the adopted reduction procedures before assembly. The contact conditions at the blade–disk interface were represented through compatibility constraints applied only at the nodes identified as active from pressure film measurements, while blade mistuning was introduced by perturbing the free-interface eigenvalue matrix of each blade substructure according to the experimentally measured blade frequencies.

The final validation against the full assembly measurements demonstrated that the proposed mistuned ROM is able to accurately reproduce both the natural frequencies and the mode shapes of the mistuned bladed disk. For the 82 mapped modes, the mistuned ROM achieved a mean absolute frequency error of 0.72% and a mean MAC value of 0.82, showing very good overall agreement with the experiments. In addition, the detailed examination of representative modes confirmed that the model is able to reproduce both tuned-like mode shapes with recognizable nodal diameter patterns and strongly localized modes that are intrinsic to mistuned systems. Even in the least favorable investigated case, the model was still able to capture the dominant spatial trend and identify the blade with the maximum response.

A further important result of this work is the comparison with the tuned ROM. While the tuned model was able to reproduce the general trend of the frequency distribution, it showed significantly poorer predictive capability, especially in terms of mode shapes. In particular, the mistuned ROM reduced the mean absolute frequency error by about 31% with respect to the tuned ROM, while the mean MAC increased by about 134%. This comparison clearly demonstrates that the explicit inclusion of both blade and contact mistuning is essential for a realistic description of the system dynamics, and especially for the prediction of localized mode shapes, which cannot be captured by an ideally tuned representation.

Overall, the proposed framework proves to be an effective and physically interpretable strategy for the dynamic analysis of mistuned bladed disks. Its main strength lies in the possibility of introducing experimentally measured blade variability directly into the ROM without modifying the reduction basis or the assembly procedure. At the same time, the method maintains a compact formulation and a substantially reduced computational cost compared to a full-order description of the assembled mistuned system. The present results therefore support the use of the FIBM method as a robust tool for the analysis and validation of mistuned bladed disk dynamics under realistic experimental conditions.

CRediT authorship contribution statement

Umidjon Usmanov: Writing – original draft, Visualization, Validation, Software, Methodology, Investigation, Formal analysis, Data curation, Conceptualization. **Christian Maria Firrone:** Writing – review & editing, Supervision, Project administration, Methodology, Investigation, Conceptualization. **Giuseppe Battiato:** Writing – review & editing, Supervision, Methodology, Investigation, Conceptualization.

Declaration of competing interest

The authors declare that they have no known competing financial interests or personal relationships that could have appeared to influence the work reported in this paper.

Data availability

Data will be made available on request.

References

[1] S.A. Tobias, R.N. Arnold, The influence of dynamical imperfection on the vibration of rotating disks, Proc. Inst. Mech. Eng. 171 (1) (1957) 669–690, URL https://doi.org/10.1243/PIME_PROC_1957_171_056_02.

[2] J.T. Wagner, Coupling of turbomachine blade vibrations through the rotor, J. Eng. Power 89 (4) (1967) 502–512, URL https://doi.org/10.1115/1.3616718.

[3] D.S. Whitehead, Effect of mistuning on the vibration of turbo-machine blades induced by wakes, J. Mech. Eng. Sci. 8 (1) (1966) 15–21, URL https://doi.org/10.1243/JMES_JOUR_1966_008_004_02.

[4] J.C. MacBain, P.W. Whaley, Maximum resonant response of mistuned bladed disks, J. Vib. Acoust. Stress. Reliab. Des. 106 (2) (1984) 218–223, URL https://doi.org/10.1115/1.3269172.

[5] D.J. Ewins, Z.S. Han, Resonant vibration levels of a mistuned bladed disk, J. Vib. Acoust. Stress. Reliab. Des. 106 (2) (1984) 211–217, URL https://doi.org/10.1115/1.3269171.

[6] J.H. Griffin, T.M. Hoosac, Model development and statistical investigation of turbine blade mistuning, J. Vib. Acoust. Stress. Reliab. Des. 106 (2) (1984) 204–210, URL https://doi.org/10.1115/1.3269170.

[7] R.C.F. Dye, T.A. Henry, Vibration amplitudes of compressor blades resulting from scatter in blade natural frequencies, J. Eng. Power 91 (3) (1969) 182–187, URL https://doi.org/10.1115/1.3574726.

[8] D. Ewins, The effects of detuning upon the forced vibrations of bladed disks, J. Sound Vib. 9 (1) (1969) 65–79, URL https://doi.org/10.1016/0022-460X(69)90264-8.

[9] D.J. Ewins, Vibration characteristics of bladed disc assemblies, J. Mech. Eng. Sci. 15 (3) (1973) 165–186, URL https://doi.org/10.1243/JMES_JOUR_1973_015_032_02.

[10] L.E. El-Bayoumy, A.V. Srinivasan, Influence of mistuning on rotor-blade vibrations, AIAA J. 13 (4) (1975) 460–464, URL https://doi.org/10.2514/3.49731.

[11] J.A. Kenyon, J.H. Griffin, Forced response of turbine engine bladed disks and sensitivity to harmonic mistuning, J. Eng. Gas Turbines Power 125 (1) (2002) 113–120, URL https://doi.org/10.1115/1.1498269.

[12] M.-T. Yang, J.H. Griffin, A reduced-order model of mistuning using a subset of nominal system modes, J. Eng. Gas Turbines Power 123 (4) (1999) 893–900, URL https://doi.org/10.1115/1.1385197.

[13] M.P. Castanier, G. Óttarsson, C. Pierre, A reduced order modeling technique for mistuned bladed disks, J. Vib. Acoust. 119 (3) (1997) 439–447, URL https://doi.org/10.1115/1.2889743.

[14] E.P. Petrov, K.Y. Sanliturk, D.J. Ewins, A new method for dynamic analysis of mistuned bladed disks based on the exact relationship between tuned and mistuned systems, J. Eng. Gas Turbines Power 124 (3) (2002) 586–597, URL https://doi.org/10.1115/1.1451753.

[15] E.P. Petrov, D.J. Ewins, Analysis of the worst mistuning patterns in bladed disk assemblies, J. Turbomach. 125 (4) (2003) 623–631, URL https://doi.org/10.1115/1.1622710.

[16] D.M. Feiner, J.H. Griffin, A fundamental model of mistuning for a single family of modes, J. Turbomach. 124 (4) (2002) 597–605, URL https://doi.org/10.1115/1.1508384.

[17] M. Kruse, C. Pierre, Forced response of mistuned bladed disks using reduced-order modeling, in: 37th Structure, Structural Dynamics and Materials Conference, American Institute of Aeronautics and Astronautics, 1996, URL https://arc.aiaa.org/doi/abs/10.2514/6.1996-1545.

[18] M.-T. Yang, J.H. Griffin, A reduced order approach for the vibration of mistuned bladed disk assemblies, J. Eng. Gas Turbines Power 119 (1) (1997) 161–167, URL https://doi.org/10.1115/1.2815542.

[19] R. Bladh, M.P. Castanier, C. Pierre, Reduced order modeling and vibration analysis of mistuned bladed disk assemblies with shrouds, J. Eng. Gas Turbines Power 121 (3) (1999) 515–522, URL https://doi.org/10.1115/1.2818503.

[20] R. Bladh, M.P. Castanier, C. Pierre, Component-mode-based reduced order modeling techniques for mistuned bladed disks: Part I — Theoretical models, in: Proceedings of the ASME Turbo Expo 2000, 2000, http://dx.doi.org/10.1115/2000-GT-0360, V004T03A006.

[21] R. Bladh, M.P. Castanier, C. Pierre, Component-mode-based reduced order modeling techniques for mistuned bladed disks: Part II — Application, in: Proceedings of the ASME Turbo Expo 2000, 2000, http://dx.doi.org/10.1115/2000-GT-0361, V004T03A007.

[22] S.H. Lim, R. Bladh, M.P. Castanier, C. Pierre, A compact, generalized component mode mistuning representation for modeling bladed disk vibration, AIAA 2 (2003) 1359–1380.

[23] P. Vargiu, C. Firrone, S. Zucca, M. Gola, A reduced order model based on sector mistuning for the dynamic analysis of mistuned bladed disks, Int. J. Mech. Sci. 53 (8) (2011) 639–646, URL https://www.sciencedirect.com/science/article/pii/S0020740311000993.

[24] T. Krizak, K. D'Souza, A generalized model of mistuning for bladed disks, J. Sound Vib. 606 (2025) 119003, URL https://www.sciencedirect.com/science/article/pii/S0022460X2500077X.

[25] S.M. Pourkiaee, S. Zucca, R.G. Parker, Relative cyclic component mode synthesis: A reduced order modeling approach for mistuned bladed disks with friction interfaces, Mech. Syst. Signal Process. 163 (2022) 108197, URL https://www.sciencedirect.com/science/article/pii/S0888327021005732.

[26] F. Mashayekhi, A. Nobari, S. Zucca, Hybrid reduction of mistuned bladed disks for nonlinear forced response analysis with dry friction, Int. J. Non-Linear Mech. 116 (2019) 73–84, URL https://www.sciencedirect.com/science/article/pii/S0020746219301179.

[27] G. Saletti, M. Pourkiaee, S. Zucca, Mass mistuning reduced order models for bladed disks with shroud friction joints, in: Proceedings of the ASME Turbo Expo 2024, 2024, http://dx.doi.org/10.1115/GT2024-123976, V10BT27A011.

[28] W. Long, Y. Chen, Reduced order modeling and mistuning identification method for rotating bladed disks under varying speeds, J. Sound Vib. 595 (2025) 118687, URL https://www.sciencedirect.com/science/article/pii/S0022460X24004498.

[29] R.R. Craig, M.C.C. Bampton, Coupling of substructures for dynamic analyses, AIAA J. 6 (7) (1968) 1313–1319, URL https://doi.org/10.2514/3.4741.

[30] S. Rubin, Improved component-mode representation for structural dynamic analysis, AIAA J. 13 (8) (1975) 995–1006, URL https://doi.org/10.2514/3.60497.

[31] R.R. Craig, A.J. Kurdila, Fundamentals of Structural Dynamics, second ed., John Wiley & Sons, Hoboken, NJ, 2006.

[32] M.S. Allen, D.J. Rixen, M. van der Seijs, P. Tiso, T. Abrahamsson, R.L. Mayes, Substructuring in engineering dynamics: Emerging numerical and experimental techniques, in: CISM International Centre for Mechanical Sciences, vol. 2020, Springer, Cham, 2020.

[33] S.N. Voormeer, Dynamic Substructuring Methodologies for Integrated Dynamic Analysis of Wind Turbines (Ph.D. thesis), Delft University of Technology, Delft, The Netherlands, 2012.
[34] T. Krizak, C.M. Firrone, G. Battiato, K. D'Souza, A bladed disk reduction technique that captures variation in blade stiffness and blade root joint contacts, ASME Turbo Expo Volume 10B: Structures and Dynamics — Fatigue, Fracture, and Life Prediction; Probabilistic Methods; Rotordynamics; Structural Mechanics and Vibration (2024) V10BT27A034. URL https://doi.org/10.1115/GT2024-129039.
[35] V. Pinto, G. Battiato, C.M. Firrone, Reduced order models for bladed disks with contact mistuning at blade root joints, in: Proceedings of the ASME Turbo Expo 2023, 2023, http://dx.doi.org/10.1115/GT2023-103078, V11BT23A006.
[36] V. Pinto, G. Battiato, C.M. Firrone, A reduction technique for the calculation of the forced response of bladed disks in the presence of contact mistuning at blade root joints, J. Eng. Gas Turbines Power 145 (2) (2022) 021013, URL https://doi.org/10.1115/1.4055722.
[37] E.P. Petrov, D.J. Ewins, Method for analysis of nonlinear multiharmonic vibrations of mistuned bladed disks with scatter of contact interface characteristics, J. Turbomach. 127 (1) (2005) 128–136, URL https://doi.org/10.1115/1.1812781.
[38] J. Avalos, M.P. Mignolet, C. Soize, Response of bladed disks with mistuned blade-disk interfaces, Turbo Expo Volume 6: Structures and Dynamics, Parts A and B (2009) 323–332, URL https://doi.org/10.1115/GT2009-59580.
[39] G. Battiao, C.M. Firrone, T.M. Berruti, B.I. Epureanu, A general method for sub-systems coupling for the dynamic analysis, in: Proceedings of ISMA 2016, Leuven, Belgium, 2016.
[40] P. Guillaume, P. Verboven, S. Vanlanduit, H. Van der Auweraer, B. Peeters, A poly-reference implementation of the least-squares complex frequency-domain estimator, Proc. IMAC 21 (2003).
[41] D.J. Ewins, Modal Testing: Theory, Practice and Application, second ed., Research Studies Press Ltd., Baldock, Hertfordshire, England, 2000.
[42] N.M.M. Maia, J.M.M. Silva, Theoretical and Experimental Modal Analysis, Research Studies Press Ltd., Baldock, Hertfordshire, England, 1997.
[43] U. Usmanov, C.M. Firrone, G. Battiato, Prediction of blade–disk contact mistuning patterns using probabilistic and machine learning methods, in: Proceedings of the ASME Turbo Expo 2026: Turbomachinery Technical Conference and Exposition, in: GT2026, American Society of Mechanical Engineers (ASME), Milan, Italy, 2026.
[44] U. Usmanov, C.M. Firrone, G. Battiato, Data-driven prediction of blade–disk contact mistuning from modal characteristics, in: Proceedings of the ASME Turbo Expo 2026: Turbomachinery Technical Conference and Exposition, in: GT2026, American Society of Mechanical Engineers (ASME), Milan, Italy, 2026.